



**UNIVERSITY OF LEEDS**

This is a repository copy of *A coupled level set and volume of fluid method with a re-initialisation step suitable for unstructured meshes*.

White Rose Research Online URL for this paper:  
<http://eprints.whiterose.ac.uk/156394/>

Version: Accepted Version

---

**Article:**

Lyras, KG, Hanson, B [orcid.org/0000-0002-1720-1656](https://orcid.org/0000-0002-1720-1656), Fairweather, M et al. (1 more author) (2020) A coupled level set and volume of fluid method with a re-initialisation step suitable for unstructured meshes. *Journal of Computational Physics*, 407. 109224. ISSN 0021-9991

<https://doi.org/10.1016/j.jcp.2019.109224>

---

© 2019, published by Elsevier Inc. This manuscript version is made available under the CC-BY-NC-ND 4.0 license <http://creativecommons.org/licenses/by-nc-nd/4.0/>.

**Reuse**

This article is distributed under the terms of the Creative Commons Attribution-NonCommercial-NoDerivs (CC BY-NC-ND) licence. This licence only allows you to download this work and share it with others as long as you credit the authors, but you can't change the article in any way or use it commercially. More information and the full terms of the licence here: <https://creativecommons.org/licenses/>

**Takedown**

If you consider content in White Rose Research Online to be in breach of UK law, please notify us by emailing [eprints@whiterose.ac.uk](mailto:eprints@whiterose.ac.uk) including the URL of the record and the reason for the withdrawal request.



[eprints@whiterose.ac.uk](mailto:eprints@whiterose.ac.uk)  
<https://eprints.whiterose.ac.uk/>

2 A coupled level set and volume of fluid method with a  
3 re-initialisation step suitable for unstructured meshes

4 Konstantinos G. Lyras<sup>a</sup>, Bruce Hanson<sup>a,\*</sup>, Michael Fairweather<sup>a</sup>, Peter J.  
5 Heggs<sup>a</sup>

6 <sup>a</sup>*School of Chemical and Process Engineering, University of Leeds, Leeds LS2 9JT, United*  
7 *Kingdom*

---

8 **Abstract**

9 This paper presents a coupling method of the level set and volume of fluid  
10 methods based on a simple local-gradient based re-initialisation approach that  
11 evaluates the distance function depending on the computational cell location. If  
12 a cell belongs to the interface, the signed distance is updated based on a search  
13 in the neighbouring cells and an interpolation procedure is applied depending on  
14 the local curvature or the sign of the level set function following [D. Hartmann,  
15 M. Meinke, W. Schröder, Differential equation based constrained reinitialisa-  
16 tion method for level set methods, *J. Comput. Phys.* 227 (2008) 6821-6845].  
17 The search algorithm does not distinguish between the upwind and downwind  
18 directions and hence it is able to be used for cells with an arbitrary number of  
19 faces increasing the robustness of the method. The coupling with the volume of  
20 fluid method is achieved by mapping the volume fraction field which is advected  
21 from the isoface evolution at a subgrid level. Consequently, the coupling with  
22 the level set approach is utilised without solving the level set equation. This  
23 coupled method provides better accuracy than the volume of fluid method alone  
24 and is capable of capturing sharp interfaces in all the classical numerical tests  
25 that are presented here.

26 *Keywords:* level set, volume of fluid, re-initialisation

---

\*Corresponding author  
*Email address:* `b.c.hanson@leeds.ac.uk` (Bruce Hanson)

## 27 **1. Introduction**

### 28 *1.1. Scope*

29 In implicit methods for calculating the interface between two fluids flowing  
30 in a fixed mesh, the interface is captured using a scalar field advected in space.  
31 The scalar field (marker) has to be intrinsically connected to the absence or  
32 presence of the liquid phase. These methods are easily extended into three-  
33 dimensions but might require fine meshes to resolve the interface. The same  
34 limitation holds for front-tracking methods. Here, we are interested in inter-  
35 faces for multiphase flows such as bubbles, droplets, and jets for liquid/liquid  
36 and liquid/gas interactions. The most commonly cited implicit methods are the  
37 volume of fluid method (VOF [1–11] and the level set (LS) methods [12–20].  
38 The level set formulation is utilised by transporting a continuous function, as  
39 in the VOF method. The level set method has been developed for an accurate  
40 representation of complex interface and boundaries for a wide range of appli-  
41 cations including among others the areas of shape optimisation [21], computer  
42 graphics [22], medical imaging [23], grid generation [24], seismology [25], and  
43 superconductors [26]. For fluid interfaces, and particularly in the two-phase  
44 flows considered in this paper, the interface of the fluid is defined by the zero-  
45 level of a signed distance function and the level set method provides an accurate  
46 representation of the curvature of the interface. One common characteristic of  
47 this method and VOF is that the user does not need to modify the method re-  
48 gardless of the complexity of the geometry since both VOF and level set adjust  
49 naturally to any topological changes. One of the main differences between the  
50 two methods, is the transition from one fluid to the other, which in the level set  
51 method occurs gradually rather than as in the volume of fluid approach where  
52 the interface exists in a one-cell layer in between the two fluids.

53 Despite its efficiency in calculating the interface, the level set method has  
54 the shortcoming that mass conservation is not guaranteed. This barrier can  
55 be overcome by coupling the method with the volume of fluid approach which  
56 is conservative, with the level set being highly accurate. This idea was im-

57 plemented first by Bourlioux [27] and Sussman and Puckett [28] giving a new  
58 method, the coupled-level-set-volume-of-fluid (CLSVOF) approach. Use of the  
59 CLSVOF showed that advecting both the volume fraction and distance func-  
60 tions can conserve mass increasing the accuracy of VOF, and providing the basis  
61 for different variations of the level set method which have been used in chemical  
62 process, aerospace and automotive industries.

63 The coupling of these two approaches does, however pose challenges for the  
64 interface reconstruction and the re-initialisation procedures that have to be ad-  
65 dressed to successfully simulate fluid flows in the case of three-dimensions or non-  
66 orthogonal meshes. In [29] a piecewise-linear interface construction/calculation  
67 (PLIC) method is described for advecting the interface, with the level set func-  
68 tion used to calculate the curvature. The volume of fluid in a computational cell  
69 defines a plane, which is constructed by the intersection points with the cell.  
70 The signed distance function is taken as the minimum distance from a finite  
71 volume centre to an interface-plane that is defined by a stencil of cells. This  
72 VOF-PLIC approach was developed for unstructured meshes in both two and  
73 three-dimensions. A similar approach was employed in [30] where the LS-VOF  
74 coupling evaluated the level set function from the minimum distance from an  
75 arbitrary cell centroid to the zero-level. In addition, no special re-initialisation  
76 process was employed, following the geometric operation proposed in [31] (the  
77 so-called coupled volume of fluid and level set, a.k.a. VOSET, method) to cal-  
78 culate the level set function near the interface. The VOSET method can be  
79 applied to accurately compute the curvature and smooth discontinuous physi-  
80 cal quantities near the interface for both structured and unstructured meshes.  
81 A different LS-VOF coupling suitable for overlapping and moving structured  
82 grids was proposed in [32] using a PLIC method for the advection of the volume  
83 of fluid approach. The interface was advected using a hybrid split, Eulerian  
84 implicit-Lagrangian explicit interface advection scheme which provided good  
85 results for the classical test of a deforming three-dimensional sphere. In [33]  
86 the idea of flux polygon reconstruction using vertex velocities was employed to  
87 evaluate the VOF function. The computed volume fraction was then corrected

88 by a flux corrector estimated using the face velocities. The level set function  
89 was advected by a high order total variation diminishing (TVD) scheme and  
90 then re-initialised in a narrow band around the interface with a geometric pro-  
91 cedure. In [34] the idea of the area of fluid was employed for advecting the  
92 volume fraction developing an iterative clipping and capping algorithm for the  
93 coupling of the level set and volume of fluid methods. Both the LS and VOF  
94 functions are advected by solving a transport equation for each one of them: the  
95 volume of fluid is advected employing an interface compression scheme whereas  
96 the LS function uses a van Leer TVD scheme. Despite its efficiency in calculat-  
97 ing the interface, the LS method has the shortcoming that mass conservation  
98 is not guaranteed. This barrier can be overcome by coupling the method with  
99 VOF approach which is conservative, and the LS which is highly accurate (see  
100 [27] and [28]). In [35] a conservative LS method was developed, which has been  
101 demonstrated to conserve mass. This has been the basis of different variations of  
102 the LS method which have been used in multiphase flows [34, 36–38]. Coupling  
103 the volume of fluid with level set it is possible to combine the benefits of both  
104 methods providing an improvement in capturing of the sharp interface with a  
105 reasonable accuracy for mass conservation. The ultimate purpose of the correct  
106 advection of the level set is the accurate calculation of curvature and mixture  
107 properties, in line with the one-fluid approach.

## 108 *1.2. Objectives*

109 This paper presents a novel coupled LS and VOF method capable of simu-  
110 lating the interface of two fluids, of different properties. The first part of the  
111 method is the re-initialisation step of the signed distance function. All tradi-  
112 tional level set methods face the problem of finding the proper values of the  
113 signed distance function,  $\psi$ , which satisfy the Eikonal equation,  $|\nabla\psi| = 1$ . This  
114 is usually done by solving the level set equation with a high order approach in  
115 time and space to minimise the error, and re-initialising the distance function  
116 to avoid the displacement of its initial value  $\psi_0$  [39]. In this paper a partial  
117 differential equation re-initialisation method is presented based on the works of

118 Russo and Smereka [40] and Hartmann et al. [41] which allows the simple and  
119 efficient calculation of the distance function across the interface. The presented  
120 formulation is second-order in space and constructed for computational cells  
121 of arbitrary shape, and is tested for both structured and unstructured meshes.  
122 The initial value of the distance function  $\psi_0$  in the coupled volume of fluid and  
123 level set methods is derived by advecting the volume fraction with either an  
124 algebraic or a geometric method. The VOF method for the research presented  
125 here, considers the motion of an isoface in a computational cell and advecting  
126 it, using the isoAdvector method proposed in [42] and implemented in the open  
127 source CFD code OpenFOAM [43]. The isoface is properly advected within a  
128 time step, estimating the volume transport across a face before moving on to  
129 the next time-step solution. The complete volume fraction advection algorithm  
130 is described in detail in the following sections. The coupling of the LS and VOF  
131 methods is developed here within OpenFOAM and is done without the need  
132 to solve the LS function equation. The approach maps the volume fraction to  
133  $\psi_0$  directly from the VOF step, and then corrects the signed distance function.  
134 In order to preserve its distance function character, the level set function is  
135 re-initialised in two parts. First, the distance function is calculated for the cells  
136 at the interface and is mapped to the level set function. In the second part the  
137 re-initialisation equation is solved for the cells adjacent to the cells at the in-  
138 terface [39, 41]. Comparisons of the VOF and the coupled LS-VOF for classical  
139 numerical tests reveal that the LS step improves the accuracy of solution and  
140 boosts the ability of the method to capture sharp interfaces.

## 141 **2. Motivation and methodology**

### 142 *2.1. Level set method*

143 The interface which separates the two fluids is represented by the level set  
144 function  $\psi(\mathbf{x}, t)$ . Depending on whether a given point  $(\mathbf{x}, t)$  with a normal  
145 distance to the interface  $d$ , exists in one fluid or the other,  $\psi(\mathbf{x}, t)$  is defined as

146  $\psi(\mathbf{x}, t) = +d$ , or  $\psi(\mathbf{x}, t) = -d$ , respectively. The interface  $\Gamma$  is then defined as  
 147 the set of points that belong to the zero-level, as follows

$$\Gamma = \{\mathbf{x} | \psi(\mathbf{x}, t) = 0\} \quad (1)$$

148 The level set function is then a distance function that is defined wherever an  
 149 interface exists. The distance function can be advected using

$$\frac{\partial \psi}{\partial t} + \mathbf{u} \cdot \nabla \psi = 0 \quad (2)$$

150 where  $\mathbf{u}$  is the velocity field. The above equation can be solved using any high  
 151 order scheme for hyperbolic systems of the ENO (essentially non-oscillatory)  
 152 schemes family or the Runge-Kutta method [44]. A similar advection equation is  
 153 used for the marker function in volume of fluid methods. Adding extra algebraic  
 154 terms to the right-hand side of this advection term, compresses the interface,  
 155 leading to conservative forms of both methods [35, 45].

## 156 2.2. Re-initialisation step

157 Although the distance function is advected well for  $\psi = 0$ , it tends to fail to  
 158 remain an actual distance function when solving Eq. (2) because of the very  
 159 small or large values the magnitude of the gradients  $|\nabla \psi|$  might attain on  
 160 either side of the interface compromising accuracy [46]. Consequently, a re-  
 161 initialisation step is required for the  $\psi$ -equation [39]. This is an extra step to  
 162 straighten the distorted shape of the function  $\psi$ , which might be caused by the  
 163 numerical solution of the convection equation or by the complicated fluid veloc-  
 164 ity fields. With the re-initialisation step the LS function and the shape of the  
 165 interface can be preserved as much as possible throughout the simulation. This  
 166 is achieved by solving the following Eikonal equation [15]

$$\frac{\partial \psi_d}{\partial \tau} = \text{sgn}(\psi)(1 - |\nabla \psi_d|) \quad (3)$$

167 where  $\text{sgn}()$  is the sign function. The new corrected distance function,  $\psi_d$ , is  
 168 calculated iteratively knowing  $\psi$  which is used as an initial guess in the re-  
 169 initialisation process,  $\psi_d(t = 0) = \psi$ . In Eq. (3),  $\tau$  is a fictitious time-step

170 which can be associated to the grid resolution. Previous studies suggest vari-  
 171 ous values for  $\tau$  (see [36, 41]) and  $\tau = 0.1\Delta x$  is considered in this study. The  
 172 re-initialisation equation can be solved in steady state and ideally converges  
 173 to  $|\nabla\psi_d| = 1$ . Previous numerical works have addressed the re-initialisation  
 174 problem providing algorithms for either structured [40, 41, 47] or unstructured  
 175 computational meshes [48]. In this study, we choose to incorporate and employ  
 176 for unstructured meshes the algorithm of [41], which is a partial differential equa-  
 177 tion based localised method, which imposes the zero-displacement constraint on  
 178 the zero LS. If  $d_P$  is the desired signed distance function at the interface for cell  
 179  $P$ , then  $d_P$  is the value of  $\psi$  that has to be used to properly advect the LS func-  
 180 tion. An initial guess,  $\tilde{d}_P$  of the distance is required during the re-initialisation  
 181 step. In [40] a central difference scheme was suggested based upon the knowl-  
 182 edge of the upwind or downwind cells of cell  $P$ . However, in [41] a modified  
 183 expression for  $\tilde{d}_P$  was utilised by imposing additional conditions that depend  
 184 on how the LS changes along the three co-ordinate directions  $x, y$  and  $z$ . In  
 185 this present study, the distance function is calculated first for the cells at the  
 186 interface and is then used to update the level set function. This is done using  
 187 first order expressions as proposed in [40]. The Eikonal equation for  $\psi$  is then  
 188 solved in a narrow band of cells adjacent to the cells that belong to the interface  
 189 [41]. The algorithm starts by searching for all the cells at the interface  $\Gamma$  of the  
 190 two fluids and performing the re-initialisation step. The algorithm is as follows:  
 191 Step 1: For all cells  $P$  at the interface  $\Gamma$ , the signed distance function  $\tilde{d}_P$  is esti-  
 192 mated first using the values of the level set function before the re-initialisation,  
 193 denoted for cell  $P$  by  $\tilde{\psi}_P$ . It can be written that

$$\tilde{d}_P = \tilde{\psi}_P / \left[ \sum_{\zeta} (\partial_{\zeta} \tilde{\psi}_{\zeta})^2 \right]^{1/2} \quad (4)$$

194 ,where  $\partial_{\zeta} \tilde{\psi}_{\zeta}$  is the discrete derivative in the  $\zeta$  direction [47]. The maximum  
 195 between the central and upwind differences can be used for calculating the  
 196 derivatives in this expression [40]. In the present study, upwind differences  
 197 are considered, employing some of the neighbouring cells. First, a search is



198 performed for all the faces  $f$  of the cell  $P$  and if a neighbouring cell  $N$  that shares  
 199  $f$  with  $P$  also belongs in  $\Gamma$ , the discrete derivative of  $\tilde{\psi}_P$ ,  $\partial_f \tilde{\psi}_P$ , is calculated  
 200 as:

$$\partial_f \tilde{\psi}_P = \frac{\tilde{\psi}_P - \tilde{\psi}_N}{x_P - x_N} \quad (5)$$

201 Let the number of all these  $\Gamma$ -neighbours be  $N_{P,\Gamma}$ . Then we use  $N_{P,\Gamma}$  discrete  
 202 derivatives. In the case of both upwind ( $\tilde{\psi}_{i-1}$ ) and downwind ( $\tilde{\psi}_{i+1}$ ) cells be-  
 203 longing to the set  $\Gamma$ , then both differences are considered in the expression for  
 204  $\tilde{d}_P$ . Since,  $2[(\partial_{i-1} \tilde{\psi}_{i-1})^2 + (\partial_{i+1} \tilde{\psi}_{i+1})^2] \geq [(\tilde{\psi}_{i+1} - \tilde{\psi}_{i-1})/\Delta x]^2$ , and given the  
 205 fact that we cannot have more than  $\lfloor N_{P,\Gamma}/2 \rfloor$  pairs of such central differences,  
 206 the sum of all these central differences for cell  $P$  in  $x, y, z$  (the right part of  
 207 the above inequality) will be no greater than the quantity in the denominator  
 208 of the signed distance function  $\tilde{d}_P$  in Eq.(4), considering all the  $N_{P,\Gamma}$  faces e.g.  
 209  $N_{P,\Gamma} \left[ \sum_f (\partial_f \tilde{\psi}_f)^2 \right]^{1/2}$ . For the tests presented here, we use this expression for  
 210 calculating  $\tilde{d}_P$ . We use these  $N_{P,\Gamma}$  derivatives to calculate the target value of  
 211 the LS which can be written as:

$$\tilde{d}_P = \frac{\tilde{\psi}_P}{(N_{P,\Gamma} \sum_{k=1}^{N_{P,\Gamma}} (\partial_{f_k} \tilde{\psi}_{f_k})^2)^{1/2}} \quad (6)$$

212 Note that the summation in Eq.(6) is performed through the cell faces and thus  
 213  $N_{P,\Gamma}$  is less than or equal to the number of faces of the cell  $P$ . The above  
 214 expression for  $\tilde{d}_P$  is bounded by the special case of a three-dimensional struc-  
 215 tured mesh introduced in [41] for Cartesian meshes with pre-defined directions,  
 216  $x, y, z$ . The upwind discretisation was employed in [41, 47] and was proven capa-  
 217 ble of avoiding any oscillations at the interface that could be caused by central  
 218 differences.

219 Step 2: The following step is performed for all the cells in  $\Gamma$  that have  
 220 negative curvature  $\kappa$  (calculated from the interface normal  $\mathbf{n}$ ,  $\kappa = \nabla \cdot \mathbf{n}$ ) or  
 221 satisfy the condition  $\kappa = 0$  and  $\tilde{\psi} \leq 0$ , (following [41]). A search is considered  
 222 for all the neighbouring cells that share the same face  $f_k$  with cell  $P$  that have  
 223 an opposite sign for  $\psi_P$  (for instance, the neighbours  $N_1, N_2$  in Fig.1). Let

224 the number of these cells be  $M_P$ , then, the signed distance function and LS  
 225 functions  $d_P, \tilde{\psi}_P$  for the cell-centre  $P$  are interpolated with the same second-  
 226 order operator as in [41] as:

$$\begin{aligned} (d)_P &= \frac{1}{M_P} \sum_{k=1}^{M_P} d_{f_k} \\ (\tilde{\psi})_P &= \frac{1}{M_P} \sum_{k=1}^{M_P} \tilde{\psi}_{f_k} \end{aligned} \quad (7)$$

229 Assuming that the ratio of the LS function with its interpolated value re-  
 230 mains the same as the ratio of the signed distance value with its interpolated  
 231 value, the position of the zero-level is fixed (a constraint imposed in [41]). The  
 232 target value of the LS function is then calculated as [41, 47]

$$d_P = \tilde{\psi}_P \frac{\sum_{k=1}^{M_P} d_{f_k}}{\sum_{k=1}^{M_P} \tilde{\psi}_{f_k}} \quad (8)$$

234 where the summation in Eq.(8) is performed over all the  $M_k$  cells that are  
 235 neighbours of the cell  $P$ , at a face  $f_k$  with a corresponding  $d_{f_k}$ , such that  
 236  $\psi_P \psi_{f_k} \leq 0$  ( $\psi_{f_k}$  is calculated at the cell centre of the neighbouring cell).

237 Step 3: The LS function for cell  $P$  is updated at the interface according to  
 238  $\psi_P = d_P$ , as suggested by [41].

239 Step 4: The re-initialisation equation is solved for the rest of the cells ad-  
 240 jacent to the interface  $\Gamma$  but with a marker function value equal to 0 or 1 (see  
 241 Fig.2). Eq. (3) is then solved in steady state:

$$\psi^{n+1} = \psi^n - \Delta \tau S(\tilde{\psi})(|\nabla \psi| - 1) \quad (9)$$

242 where  $S(\tilde{\psi}) = \tilde{\psi} / \sqrt{\tilde{\psi}^2 + |\nabla \tilde{\psi}|^2 \Delta x^2}$  is a modification of the sign function and  
 243  $\Delta x$  is the cell size. The gradient magnitude is  $|\nabla \psi| \cong H_G(D_\zeta^- \psi^n, D_\zeta^+ \psi^n)$  is the  
 244 Godunov-Hamiltonian of the LS function from the previous iteration through  
 245 all faces of the particular cell. Here, the terms  $D_\zeta^- \psi^n, D_\zeta^+ \psi^n$  are the first or-  
 246 der approximations of the gradient of  $\psi$  along the  $\zeta$ -direction,  $\zeta = x, y$  or  $z$

247 depending on whether the upwind "-" or the downwind cell is considered "+"

$$248 \quad D_{\zeta}^{-} \psi^n = \frac{\psi_i^n - \psi_{i-1}^n}{\Delta \zeta}, \quad D_{\zeta}^{+} \psi^n = \frac{\psi_{i+1}^n - \psi_i^n}{\Delta \zeta} \quad (10)$$

249

250 The need to use first order terms arises from the large gradients across the inter-  
 251 face that require an accurate and stable method of calculating  $H_G$ . The above  
 252 formulation is the basis for various fast marching algorithms with structured  
 253 meshes, e.g. [15, 28, 41]. Here, the normal gradient of the level set function  $\nabla_f^{\perp}$   
 254 is calculated for all the faces  $f$  based on the orientation of the normal at the  
 255 face. In general

$$\nabla_f^{\perp} = \alpha_{corr}(\psi_P - \psi_n)/|\Delta \zeta| \hat{\zeta} + (\hat{\zeta} - \alpha_{corr} \Delta \zeta) \nabla(\psi)_f \quad (11)$$

256 where  $\alpha_{corr}$  is the inverse cosine of the angle between the cell centres and the  
 257 normal face, and  $\nabla(\psi)_f$  is the linearly interpolated gradient at the face  $f$ . This  
 258 expression is used for meshes that non-orthogonality is high, and for orthogonal  
 259 meshes the second part of the right-hand-side is omitted. Following [34] in the  
 260 case of unstructured meshes, one possible approach is to select the upwind cell  
 261 from all face-neighbouring cells of the central cell  $P$  as the one whose centre  
 262 position is closest to the line through the centre and downwind nodes. If the  
 263 position vector is  $\Delta \zeta$  and the unit vector is denoted as  $\hat{\zeta}$ , then if  $\psi < 0$  and  
 264  $\Delta \zeta \cdot \hat{\zeta} < 0$  or  $\psi > 0$  and  $\Delta \zeta \cdot \hat{\zeta} > 0$  we have:

$$a_{\zeta} = \min \left( \nabla_f^{\perp} \psi \cdot \hat{\zeta} \right) \quad (12)$$

265 If  $\psi < 0$  and  $\Delta \zeta \cdot \hat{\zeta} > 0$  or  $\psi > 0$  and  $\Delta \zeta \cdot \hat{\zeta} < 0$  then:

$$a_{\zeta} = \max \left( \nabla_f^{\perp} \psi \cdot \hat{\zeta} \right) \quad (13)$$

266 The Hamiltonian-Godunov term is simply calculated as

$$H_G = \sqrt{\max(a_x^2) + \max(a_y^2) + \max(a_z^2)} \quad (14)$$

267 For the test cases presented here, no significant difference was observed using  
 268 an explicit calculation of the gradient of  $\psi$  in Eq. (9). This can be performed for

269 unstructured meshes for a cell  $P$  with volume  $V^{(P)}$ , faces  $f$  and surface vector  
 270  $\mathbf{S}_f$  using:

$$\nabla\psi_d^{(P)} = \frac{1}{V^{(P)}} \sum_f \psi_f \mathbf{S}_f \quad (15)$$

271 The steady solutions of Eq. (9) are distance functions. Furthermore, since  
 272  $\text{sgn}(0) = 0$ , then  $\psi_d(\mathbf{x}, \tau)$  has the same zero-level as  $\psi$ .

273 The fictitious time step for the steady state iterations  $\Delta\tau$ , has to be chosen  
 274 so that an accurate value of the LS function is obtained within a reasonable  
 275 number of iterations.  $\Delta\tau$  can be a fraction of or equal to the mesh size,  $\Delta x$   
 276 [34, 40]. For the simulations performed in this study,  $\Delta\tau = 0.1(\Delta x \Delta y \Delta z)^{\frac{1}{3}}$  has  
 277 been chosen.

278 A fixed small number of iterations is needed in practice to guarantee the  
 279 distance function property near the interface. Following [46], the number of  
 280 iterations depends on the thickness of the interface  $2\epsilon\Delta x$ , with  $\epsilon$  being the layer  
 281 of cells across which the re-initialisation step takes place (the correction is kept  
 282 local). The iteration process can stop after  $2\epsilon$  time-steps, and a value of  $\epsilon = 1.5$   
 283 is chosen here so that the interface is spread over a thickness of three cells  
 284 (see also Step 4). Finally, for both formulations, Eq.(3) and Eq.(9), the initial  
 285 value  $\psi_0(\mathbf{x}) = \psi(\mathbf{x}, 0)$  can be taken from the volume fraction  $\alpha$  assuming the  
 286 interface position is at the iso-surface contour  $\alpha=0.5$ , (as in [49]) and is written  
 287 as a function of the cell size [36].

### 288 *2.3. Utilising the one-fluid approach*

289 Having calculated the LS function, the mixture properties such as density  
 290 and viscosity can be evaluated with the one-fluid approach. The two fluids are  
 291 treated as one fluid with properties that change across the interface [7]. To  
 292 achieve numerical robustness, a smeared Heaviside function,  $H$ , is used [35]  
 293 defined as

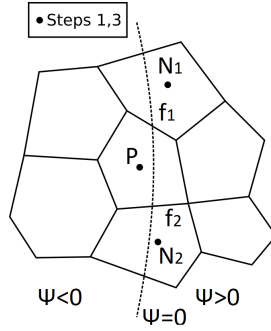


Figure 1: Steps 1-4 performed for a computational cell  $P$  in a non-uniform two-dimensional mesh.

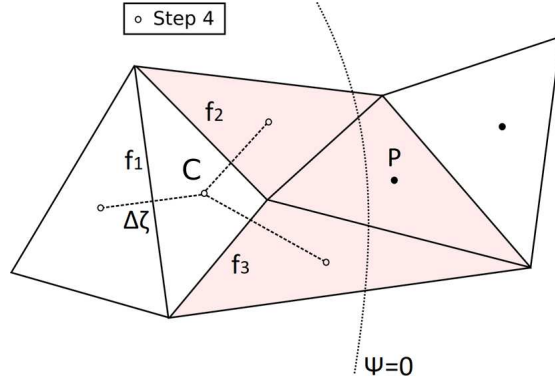


Figure 2: Step 4 performed for a computational cell  $C$  that does not belong to  $\Gamma$ .

$$H(\psi) = \begin{cases} 0 & \text{if } \psi < -\epsilon \\ \frac{1}{2} \left[ 1 + \frac{\psi}{\epsilon} + \frac{1}{\pi} \sin\left(\frac{\pi\psi}{\epsilon}\right) \right] & \text{if } |\psi| \leq \epsilon \\ 1 & \text{if } \psi > \epsilon \end{cases} \quad (16)$$

294 The pseudo-fluid properties can be then calculated as

$$\rho = \rho_1 H + \rho_2 (1 - H) \quad (17)$$

$$\mu = \mu_1 H + \mu_2 (1 - H) \quad (18)$$

295 The surface tension force acting on the interface is calculated as [36, 50]

$$F_\sigma = \sigma \kappa \delta(\psi) \nabla \psi \quad (19)$$

296 Here  $\delta()$  is the Dirac function which is employed for limiting the effect of the  
 297 surface tension force in the vicinity of the interface, a region with thickness  $\epsilon$

$$\delta(\psi) = \begin{cases} 0 & \text{if } |\psi| > \epsilon \\ \frac{1}{2\epsilon} \left[ 1 + \cos\left(\frac{\pi\psi}{\epsilon}\right) \right] & \text{if } |\psi| \leq \epsilon \end{cases} \quad (20)$$

298 The curvature and the gradient can be discretised (since  $\psi$  is a continuous  
 299 function) and the surface tension can be calculated at the cell faces using

$$F_\sigma = (\sigma \kappa)_f \delta_f(\psi) \nabla_f^\perp \psi \quad (21)$$

#### 300 2.4. Numerical formulation of coupling Volume of fluid and level set methods

301 The initial value  $\psi_0$  used in Eq. 3 is the starting point for the re-initialisation  
 302 iterations and the link with the VOF method. A straightforward approach  
 303 without solving the LS equation [36, 49] is to use

$$\psi_0 = (2\alpha - 1) \tilde{\Delta} x \quad (22)$$

304 In the above initial value the  $\alpha - 0.5$  iso-surface is used as a starting point for  
 305 the signed distance function. The percentage of the interface thickness,  $\tilde{\Delta} x$   
 306 here equal to  $0.8\Delta x$ , is introduced for numerical robustness and gives a  $\psi_0$   
 307 value within  $(-\epsilon, \epsilon)$  for the cells belonging to  $\Gamma$ . The volume fraction  $\alpha$  can be  
 308 advected with various methods [46, 51–53]. The advection of the volume fraction  
 309 depends on the normal to the interface, usually performed employing values in  
 310 the neighbouring cells by selecting the orientation of the interface. The coupling  
 311 methods used with the VOF approach in [34, 36] use a transport equation for  
 312 the volume fraction with the MULES limiter. Even with the addition of an  
 313 extra term for compressing the interface,  $\alpha(1 - \alpha)U_r$ , where  $U_r$  is the relative  
 314 velocity between the two fluids [45], the interface might still diffuse as previously

315 shown in numerical tests in [30, 42], which can be limited, coupling this scheme  
 316 with a level set method [34].

317 The approach in [42] is used to advect the volume and the surface submerged  
 318 in one fluid inside each cell at the interface. The idea is that after every time-  
 319 step, the iso-surface inside a computational cell (at  $\Gamma$ ) splits the cell  $C$  with  
 320 volume  $V_C$  into two different parts: one occupied by fluid 1 with volume frac-  
 321 tion  $\alpha$  and the other one filled with fluid 2 with volume fraction  $(1 - \alpha)$ . Let  
 322  $X_1, X_2, \dots, X_k$  be the nodes of a cell at the interface, as in Fig.3. The sub-grid  
 323 face defined from the line connecting all the intersection points  $x_m$  of the iso-  
 324 surface and the cell edges, the isoface, is assumed to be advected with a velocity  
 325 equal to the velocity of the previous time step and is calculated by solving the  
 326 momentum equation. The points  $x_m$  at a cell edge  $(X_k X_l)$  can be evaluated  
 327 from

$$328 \quad x_m = X_k + \lambda_\alpha(X_l - X_k) \quad (23)$$

329 where  $\lambda_\alpha$  is a weight function defined by interpolating at each node  $X_i$  the vol-  
 330 ume fraction of the surrounding cells. Hence,  $\lambda_\alpha = (\alpha - \alpha_k)/(\alpha_l - \alpha_k)$ , where  
 331  $\alpha_k, \alpha_l$  are the corresponding values at the nodes  $X_k, X_l$ . With this linear in-  
 332 terpolation the isoface will split the cell into one subcell of fluid 1 with volume  
 333  $\Delta V_C(\alpha)$  and another one with volume  $V_C - \Delta V_C$  of fluid 2. The isoAdvect  
 334 method of Roenby et al. [42] is then performed to find the optimum isovalue  
 335  $\alpha^*$  such that  $\alpha = \Delta V_C(\alpha^*)/V_C$ . A proper value of  $\alpha^*$  will cut the cell  $C$  into  
 336 two subcells with volumetric proportions calculated from the previous guess of  
 337 the volume fraction  $\alpha_C$  leading to a more accurate reconstruction of the inter-  
 338 face than would be obtained using the 0.5-isovalue. The procedure resembles  
 339 the re-initialisation step in the correction of the LS method. Using a third  
 340 degree polynomial  $p_\alpha(x)$  for interpolating the isovalue, we have the following

341 constraints:

$$\begin{aligned}
 & p_\alpha(x_k) = f_k \\
 & p_\alpha\left(x_k + \frac{x_k - x_l}{3}\right) = \frac{f_k}{3} \\
 & p_\alpha\left(x_k + \frac{2(x_k - x_l)}{3}\right) = \frac{2f_k}{3} \\
 & p_\alpha(x_l) = f_l
 \end{aligned}
 \tag{24}$$

343  
 344 Finding the polynomial that passes through these points, can then be used to  
 345 calculate the isovalue and the isoface which are now defined since both the  
 346 vertices and its area,  $E_m$ , are known.

347 Next step, is the time evolution of the isoface within a cell. The isoface will  
 348 have a centre  $x_c$  and velocity  $\mathbf{u}_c$  with a normal vector  $\mathbf{n}_c$ , as in Fig.3. The  
 349 isoface will then pass all the vertices  $X_k$  at time  $t_k$  which is calculated in [42]  
 350 from

$$t_k = t + \mathbf{dx}_i \cdot \frac{\mathbf{n}_c}{\mathbf{u}_c} \tag{25}$$

351 where the vector  $\mathbf{dx}_k$  connects the isoface centre with the vertices,  $\mathbf{dx}_k =$   
 352  $X_k - x_c$ . Knowing the time  $t_k$  allows calculation of the face-interface line during  
 353 the solution time step  $\delta t$ . The submerged area can be integrated using all the  
 354 time integrals  $[t_k, t_{k+1}]$  such that  $t < t_k, t_{k+1} < t + \delta t$ . If there are  $N_{sub}$  such  
 355 time steps then:

$$\int_t^{t+\delta t} E_m d\tau' = \sum_{k=1}^{N_{sub}} \int_{t_k}^{t_{k+1}} E_m d\tau' \tag{26}$$

356 The volume of the fluid with the isoface  $E_m$  is easily calculated, since:

$$\Delta V_f^n = \frac{\phi_f}{|\mathbf{S}_f|} \sum_{k=1}^{N_{sub}} \int_{t_k}^{t_{k+1}} E_m d\tau' \tag{27}$$

357 using the volumetric fluxes and the face area at face  $f$ ,  $\phi_f$  and  $|\mathbf{S}_f|$ . The volume  
 358 fraction is then updated explicitly using the transported volume at each face as

$$\alpha^{t+\delta t} = \alpha^t - \frac{1}{V_C} \sum_{f=1}^{N_f} \Delta V_f^n \tag{28}$$



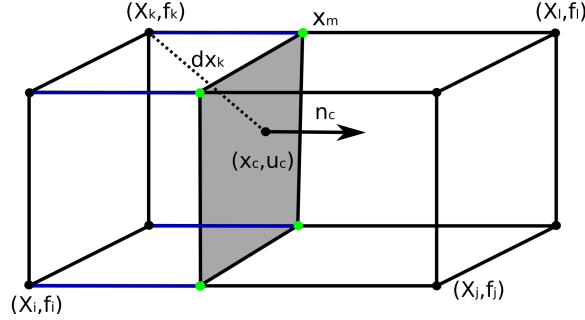


Figure 3: Isoface advection step inside a computational cell. Isoface nodes within the interval  $[t_k, t_{k+1}]$  (green points), isoface (shaded face) and face-interface lines (blue).

359 The coupling algorithm of this isoface-level-set-volume-of-fluid (ILSVOF)  
360 method can be described in the following main steps. The numerical fields are  
361 initialised together with the LS function. The dynamic pressure is used to avoid  
362 any sudden changes in the pressure at the boundaries for hydrostatic problems.  
363 The time loop starts by correcting the interface and the volume fraction at the  
364 boundaries. The volume fraction is advected, and corrected, and new values of  
365  $\alpha$  are assigned at the boundaries. The new LS function  $\psi_0$  is calculated using  
366 the results of the advection equation. Next,  $\psi$  is re-initialised applying Steps  
367 1-4 described for the re-initialisation procedure, to obtain the signed distance  
368 function, and the interface at the boundaries is corrected. The new interface  
369 curvature is calculated. The mixture properties and fluxes are updated using the  
370 LS function. For instance, for density  $\rho = \rho_1 H + \rho_2(1 - H)$  is used, where  $H()$   
371 is a Heavyside function of  $\psi$  which is used instead of  $\psi$  for numerical purposes  
372 in LS methods, [35]. The Navier-Stokes equations are solved for velocity and  
373 pressure using the pressure implicit with splitting of operators (PISO) method.  
374 The process starts again, by first correcting the interface and the volume fraction  
375 at the boundaries and then, following the described steps after that.

376 **3. Numerical tests and discussions**

377 The performance of the proposed numerical methodology is tested using  
378 simple test problems involving two fluids of different densities and viscosities.  
379 The problems, in both two and three-dimensions, include comparisons between  
380 the presented method and other numerical works with or without the level set  
381 implementation. Different indicators are used for monitoring the method’s per-  
382 formance in terms of shape conservation and boundedness. The numerical tests  
383 presented here concern both structured and unstructured meshes and different  
384 mesh resolutions are examined for the presented test cases.

385 *3.1. Two-dimensional rotating disc*

386 The rotating disc has been proposed in [54] and considers a disc that under-  
387 goes a significant interface deformation and is used here to evaluate the abil-  
388 ity of the presented methodology to transport under-resolved interface struc-  
389 tures [6, 9, 33, 55]. The computational domain is a unit square which con-  
390 tains a disc with radius  $R$  placed in the domain so that the disc centre is at  
391  $(x, y) = (0.5, 0.75)$ . The rest of the domain is filled with a fluid of lower viscosity  
392 than the one of the disc. The velocity field is given by

$$u(x, y, t) = -\sin^2(\pi x)\sin(2\pi y)\cos\left(\frac{\pi t}{T}\right) \quad (29)$$

$$v(x, y, t) = \sin(2\pi x)\sin^2(\pi y)\cos\left(\frac{\pi t}{T}\right) \quad (30)$$

393 The velocity field changes in time and space and causes the disc to rotate so that  
394 the initially circular disc is stretched with time (the flow lasts for one period  $T$ ).  
395 The resulting filament will then stretch until  $t = T/2$  at which point the velocity  
396 field reduces to its minimum and becomes zero, according to Eq. (29). For the  
397 simulations here, a period of  $T = 8$  was used with a total simulation time of  $8s$ .  
398 The physical parameters considered are summarised in Table 1. Two different  
399 types of mesh have been used, quadrilateral and triangular, as the ones shown  
400 in Fig. 4 each using a coarse, medium and a fine meshes respectively. The

401 results for the new method are shown in Tables 2 and 3. A comparison of  
 402 the ILSVOF methodology described here, with the case of using only the VOF  
 403 method [42] without the level set, is also included. Previous studies in [42]  
 404 have shown that the volume of fluid method of [42] provides higher accuracy for  
 405 interface advection than the volume of fluid approach of [45] based on, hence  
 406 only the error in shape preservation reported in [42] is included for comparisons  
 407 in Tables 2 and 3. Some results obtained using only [45] approach for two and  
 408 three-dimensional cases are presented for qualitative comparisons in Fig. 5. The  
 409 error

$$E_\alpha = \frac{\sum_i V_i |\alpha_i - \alpha_{exact}|}{\sum_i V_i \alpha_{exact}} \quad (31)$$

410 is used as a quantitative measure of the shape preservation. Here, the exact  
 411 solution is defined as the initial position of the rotating disk and  $E_\alpha$  is calculated  
 412 over all cells of the domain. The extent to which the solution stays within the  
 413 range of physical values is also tested, considering the minimum and maximum of  
 414 the liquid volume fraction of the rotating disc,  $\min(\alpha)$  and  $\max(\alpha)$  respectively,  
 415 also calculated over all cells of the domain. One should expect ideally to have  
 $0 \leq \alpha \leq 1$  for all cells.

Table 1: Physical properties for rotating disc simulations.

	Physical and numerical parameters
Heavy fluid density	1110 $kg/m^3$
Light fluid density	806 $kg/m^3$
Heavy fluid kinematic viscosity	1.017e-06 $m^2/s$
Light fluid kinematic viscosity	2.35e-06 $m^2/s$
Length of square domain	1 $m$
Period $T$	8 $s$
CFL number	0.3

416

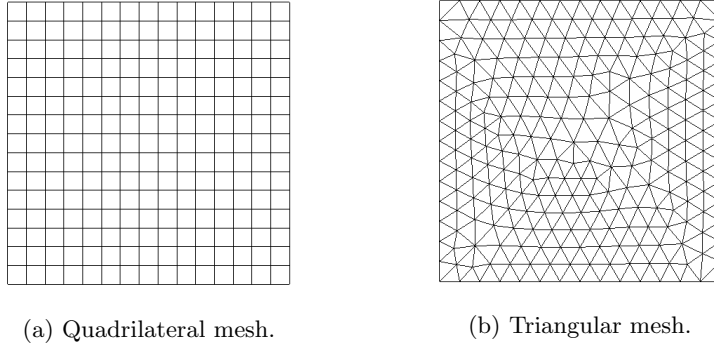


Figure 4: Meshes used to discretise the domain used (coarse mesh study).

417 As indicated in the results of Fig. 5, increasing the mesh resolution, increases  
 418 the sharpness of both methods with  $E_\alpha$  decreasing. The mesh resolution is  
 419 a important parameter that influences the ability of the interface capturing  
 420 method to resolve the ligament stretching. The sharp tail at the end of the  
 421 deforming ligament fails to be resolved at the subgrid scale. In all cases, at  
 422 the time of maximum stretching,  $t = T/2$ , the rotating spiral thickness becomes  
 423 equivalent to the local cell size and fragmentation starts to be noticeable (Fig. 5).  
 424 The observed volume sharpness error was generally of the same order as that  
 425 obtained from the other approaches, or smaller. The same behaviour is observed  
 426 in boundedness were the marker function,  $\alpha$ , stays above the minimum value of  
 427 0 and below or equal to 1, contrary to the solution obtained without the level  
 428 set step. The ILSVOF method maintains similar trends for the error measures  
 429 for both structured and unstructured meshes (Table 3). A comparison between  
 430 the presented ILSVOF and the VOF methods is shown for  $t = T/2$  in Fig. 6 for  
 431 the case of the medium size quadrilateral meshes using the OpenFOAM VOF  
 432 methods of [42] and [45] which employs the multidimensional universal limiter  
 433 with explicit solution (MULES) scheme [56]. As the rotating vortex thickness  
 434 becomes progressively smaller, the droplets pinch off and the local interface  
 435 curvature becomes of the same order as the mesh size. The decreasing interface  
 436 curvature causes the isoface, used here to advect  $\alpha$ , to become less accurate for

437 the resulting droplet motion. The coupling with level set shows that it is possible  
438 to have less diffusion at the tip for the rotating filament for both quadrilateral  
439 and triangular meshes (Fig. 7). The gradients appearing during the deformation  
440 of the vortex might have an effect on shape preservation, via Eq. (6), even though  
441 the vortex reverses after  $t = T/2$  back to its initial position, but these do not  
442 seem to reduce the solution accuracy, at least for the re-initialisation steps used  
443 here which usually varied from 2 to 5. The ILSVOF retains the vortex shape  
444 better than the other methods at the maximum stretching position. Using  
445 the interface compression scheme MULES, sharpness can also be maintained  
446 at  $t = T/2$ , but this interface compression might cause the rotating spiral to  
447 break-up, fragmenting the vortex in the interval  $[T/2, T]$  which is more evident  
448 at  $t = T$  in Fig. 6 and Fig. 7. The increased error in the averaged volume  
449 fraction for this approach is also reported in previous studies in [34], and is  
450 observed here in both structured and unstructured methods.

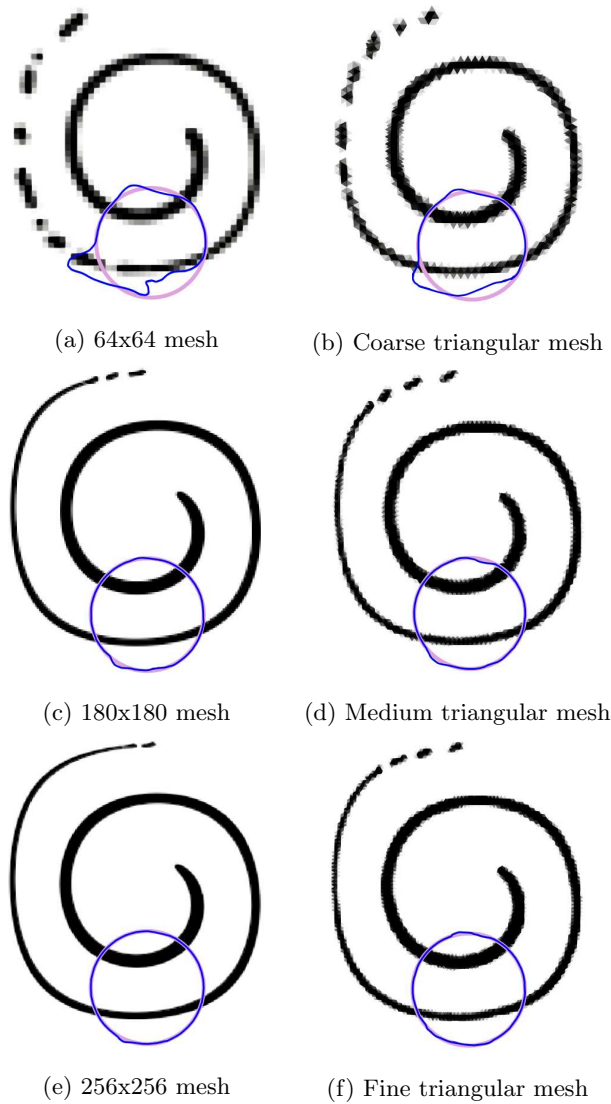


Figure 5: Two-dimensional rotating disc test for level set-VOF method at  $t = T/2$ . The initial (light purple line) at  $t = 0$  and final position of the zero-level set iso-surface (blue line) at  $t = T$  are indicated.

451 Comparisons with different grid resolutions ( $32^2, 64^2, 128^2$ ) are shown in Ta-  
 452 ble 4 for the values of the calculated  $L_1(\alpha)$  error norm for the volume fraction.  
 453 Results for  $L_1(\alpha)$  from other numerical works are included for comparisons and

Table 2: Comparison of the methods using quadrilateral meshes for the two-dimensional rotating disc case.

Mesh resolution	ILSVOF method			VOF method		
	$E_a$	$\min(\alpha)$	$\max(\alpha)$	$E_a$	$\min(\alpha)$	$\max(\alpha)$
$64^2$	$-1.03 \times 10^{-7}$	0.0	1.0	$3.30 \times 10^{-7}$	0.0	1.0
$180^2$	$-1.58 \times 10^{-8}$	$4.60 \times 10^{-9}$	1.0	$1.2 \times 10^{-8}$	$-2.88 \times 10^{-8}$	$1.0-1.18 \times 10^{-8}$
$256^2$	$-9.61 \times 10^{-9}$	$-7.16 \times 10^{-7}$	$1.0-1.5 \times 10^{-9}$	$-2.48 \times 10^{-8}$	$-3.34 \times 10^{-5}$	$1.0-3.64 \times 10^{-8}$

Table 3: Comparisons of the methods using triangular meshes for the two-dimensional rotating disc case.

Mesh resolution	ILSVOF method			VOF method		
	$E_a$	$\min(\alpha)$	$\max(\alpha)$	$E_a$	$\min(\alpha)$	$\max(\alpha)$
17521	$-2.77 \times 10^{-7}$	0.0	1.0	$7.26 \times 10^{-7}$	$-1.14 \times 10^{-8}$	$1.0-9.61 \times 10^{-10}$
79877	$3.91 \times 10^{-8}$	0.0	1.0	$-4.34 \times 10^{-7}$	0	1.0
108151	$2.11 \times 10^{-8}$	0.0	1.0	$-1.68 \times 10^{-8}$	$-9.2 \times 10^{-8}$	$1.0-4.78 \times 10^{-8}$

454 the domain and physical properties for the rotating disc test are set as those  
455 in [57]. The method presented here, overall demonstrated good accuracy for  
456 the two-dimensional rotating vortex case. Compared to other volume of fluid  
457 methods that use PLIC such that in [6] the error in  $L_1(\alpha)$  is lower for all the  
458 meshes tested here. Compared to the tangent of hyperbola for INterface cap-  
459 turing, (THINC) scheme and its variations [57–59], the results here are similar  
460 or lower. The  $L_1(\alpha)$  error is close for the coarse mesh compared to the level  
461 set method in [60], but had lower values for the medium and fine meshes. The  
462 mass conservation error through time is shown in Fig. 8. The method showed  
463 generally reasonable mass conservation error for the different meshes that were  
464 used, as shown in Table 4.

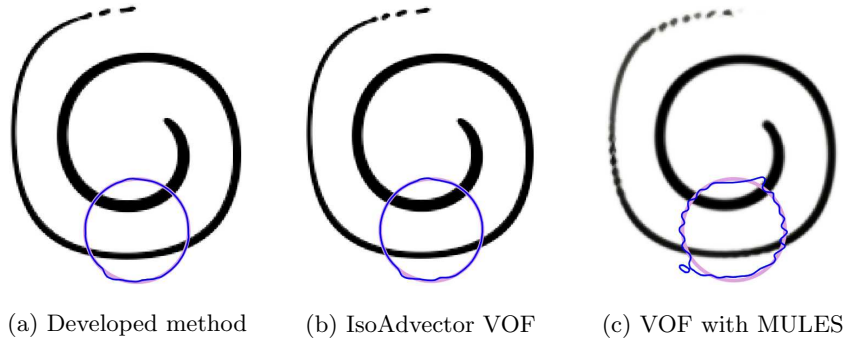


Figure 6: Two-dimensional rotating disc test for the medium quadrilateral mesh at  $t = T/2$ . The initial (light purple line) at  $t = 0$  and final position of the zero-level set iso-surface (blue line) at  $t = T$  are indicated.

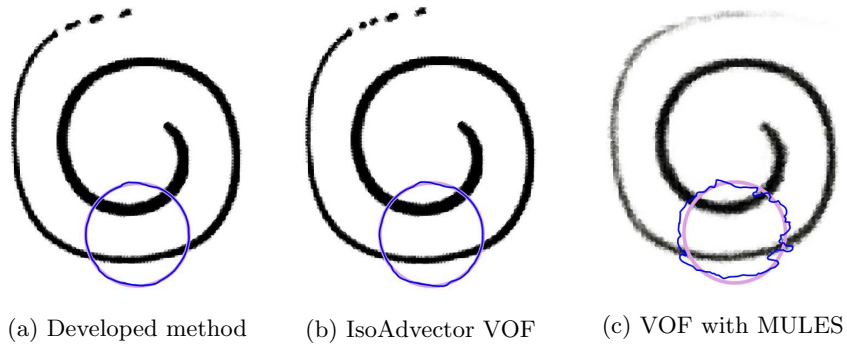


Figure 7: Two-dimensional rotating disc test for the fine triangular mesh at  $t = T/2$ . Initial (light purple line) at  $t = 0$  and final position of the zero-level set isosurface (blue line) at  $t = T$  are indicated.



Table 4: Comparisons of the methods using quadrilateral meshes for the two-dimensional rotating disc case. The first order norm  $L_1(\alpha)$  is calculated for the three different meshes.

Authors	$32^2$	$64^2$	$128^2$
RiderKothe/Puckett [61]	$4.78 \times 10^{-2}$	$6.96 \times 10^{-3}$	$1.44 \times 10^{-3}$
THINC/WLIC [57]	$4.16 \times 10^{-2}$	$1.61 \times 10^{-2}$	$3.56 \times 10^{-3}$
Markers-VOF [62]	$7.41 \times 10^{-3}$	$2.78 \times 10^{-3}$	$4.78 \times 10^{-4}$
DS-CLSMOF [60]	$2.92 \times 10^{-2}$	$5.51 \times 10^{-3}$	$1.37 \times 10^{-3}$
PLIC [6]	$2.53 \times 10^{-2}$	$2.78 \times 10^{-3}$	$4.8 \times 10^{-4}$
THINC/QQ [58]	$6.70 \times 10^{-2}$	$1.52 \times 10^{-2}$	$3.06 \times 10^{-3}$
THINC/SW scheme [59]	$3.90 \times 10^{-2}$	$1.52 \times 10^{-2}$	$3.96 \times 10^{-3}$
ISLSVOF method	$4.19 \times 10^{-2}$	$1.43 \times 10^{-3}$	$8.36 \times 10^{-4}$

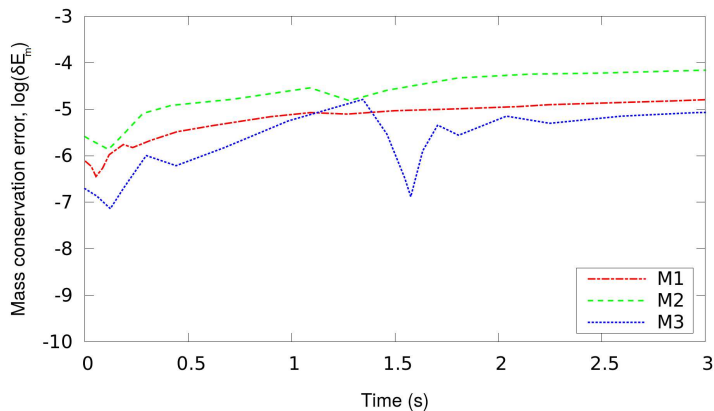


Figure 8: Mass conservation error for the two-dimensional rotating disc case for the three levels of refinement. Here, the meshes  $M_1$ ,  $M_2$  and  $M_3$  had  $32^2$ ,  $64^2$  and  $128^2$  cells respectively.

### 465 3.2. Three-dimensional rotating sphere in a non-uniform velocity field

466 The next test is the case of a three-dimensional rotating sphere of [54] and  
 467 is used to assess the capability of the methodology for capturing the interface  
 468 distortion in three dimensions. [34, 36, 42, 63]. In this test, a sphere with radius  
 469  $R = 0.15m$  is placed inside a box  $[0, 1]^3$  with its centre at  $(0.35, 0.35, 0.35)$ . The

470 velocity field is defined as

$$\begin{aligned}
 u(x, y, z, t) &= 2\sin^2(\pi x)\sin(2\pi y)\sin(2\pi z)\cos\left(\frac{\pi t}{T}\right) \\
 v(x, y, z, t) &= -\sin(2\pi x)\sin^2(\pi y)\sin(2\pi z)\cos\left(\frac{\pi t}{T}\right) \\
 w(x, y, z, t) &= -\sin(2\pi x)\sin(2\pi y)\sin^2(\pi z)\cos\left(\frac{\pi t}{T}\right)
 \end{aligned}
 \tag{32}$$

473 The period is  $T = 3s$ , and the density and viscosity of both fluids in the test,  
 474 are the same as in the previous section (see Table 1). The sphere is rotating  
 475 within the non-uniform velocity field which causes the sphere to deform through  
 476 time during  $[0, T/2]$ . At  $t = T/2$  the flow reverses due to the sign change of the  
 477 cosine parameter during  $[T/2, T]$  causing the deformed sphere to return back  
 478 to its original position at  $t = T$ . The ILSVOF method was first tested for  
 479 three different meshes (with  $40^2, 64^2, 100^2$  elements) to assess the error in shape  
 480 preservation and the boundedness of the marker function. The results given in  
 481 Table 5 compare the method with and without the level set step using structured  
 482 meshes. Overall, the error  $E_\alpha$  decreases with the level set implementation. A  
 483 slight increase in  $E_\alpha$  is observed for the fine mesh with respect to the medium  
 484 mesh, although this is relatively insignificant. Similar trends were observed by  
 485 previous authors using LS and VOF method coupling [34]. A more detailed  
 486 comparison is given in Fig. 9 at the maximum deformation time,  $t = T/2$  for  
 487 different grid resolutions ( $40^2, 64^2, 100^2, 128^2$  elements). The deforming sphere  
 488 appears to be thicker in the case of the ILSVOF method which provides more  
 489 detail for the deforming sphere for the different levels of mesh refinement. The  
 490 sharp sphere end is also thickened in the ILSVOF case, and the thickening  
 491 appears to be more evident for the finer meshes. The time evolution of the  
 492 deforming sphere inside the non-uniform flow is shown for different times within  
 493  $[0, T]$  in Fig. 10 for a  $128^3$  mesh. Numerical results revealed as before, relatively  
 494 large gradients that the LS function experiences in  $[0, T/2]$  which are maintained  
 495 and are not reversed in the interval  $[T/2, T]$  giving a perturbed profile at the final  
 496 position of the sphere. The sphere interface is distorted in all cases as shown in  
 497 Fig 11 at  $t = T$ , with or without level set or interface compression. In general,

498 the ILSVOF method shows better representation of the surface. The most  
 499 significant surface distortion is observed in the case of the interface compression  
 500 where the compression of the interface decreases the solution accuracy [34]. The  
 501 three-dimensional sphere in the same non-uniform flow was also simulated using  
 502 unstructured meshes and the results are shown in Table 6. The values of  $E_\alpha$   
 503 are higher for the medium and fine meshes compared with those in Table 5 for  
 504 structured meshes. The sheet thickness appears to be smaller than the average  
 505 edge length even for the finest tetrahedral mesh ( $\sim 0.008$ ), causing the solution  
 506 accuracy to drop in the case of unstructured meshes. In addition, the impact of  
 507 the steep gradients introduced in the LS method that originate from the initial  
 508 value of  $\psi_0$  in Eq. 22 being inserted in Eq. 3 are more evident in the case of  
 509 tetrahedral meshes. The  $L_1$  error for the volume fraction for different mesh  
 510 resolutions ( $32^3, 64^3, 128^3$ ) for the three-dimensional case of the rotating sphere  
 511 are shown in Table 7. Following [56, 59] the error  $L_1$  is calculated for all cells  $i$   
 512 and is defined as

$$L_1(\alpha) = \sum_i (\alpha_i - \alpha_{exact}) V_i \quad (33)$$

513 The results are shown alongside with the  $L_1$  error obtained with other volume of  
 514 fluid methods. The accuracy of the results here, remained lower than the volume  
 515 of fluid with the THINC/SW scheme which uses no geometrical reconstruction  
 516 [59] and was more accurate compared to the results obtained in [56] with the  
 517 MULES limiter with interFoam. In all cases the  $L_1$  error was very close to the  
 518 results from the PLIC VOF method in [64].

Table 5: Comparison of the methods using quadrilateral meshes for the three-dimensional rotating sphere case.

Grid	ILSVOF method			VOF method		
	$E_a$	$\min(\alpha)$	$\max(\alpha)$	$E_a$	$\min(\alpha)$	$\max(\alpha)$
$40^3$	$5.43 \times 10^{-7}$	$-4.05 \times 10^{-17}$	1.0	$5.84 \times 10^{-7}$	$-1.87 \times 10^{-16}$	1.0
$64^3$	$-9.85 \times 10^{-8}$	$-1.48 \times 10^{-16}$	1.0	$-1.04 \times 10^{-7}$	$-1.53 \times 10^{-9}$	$1.0-5.93 \times 10^{-11}$
$100^3$	$1.79 \times 10^{-7}$	0.0	1.0	$3.22 \times 10^{-7}$	0.0	1.0

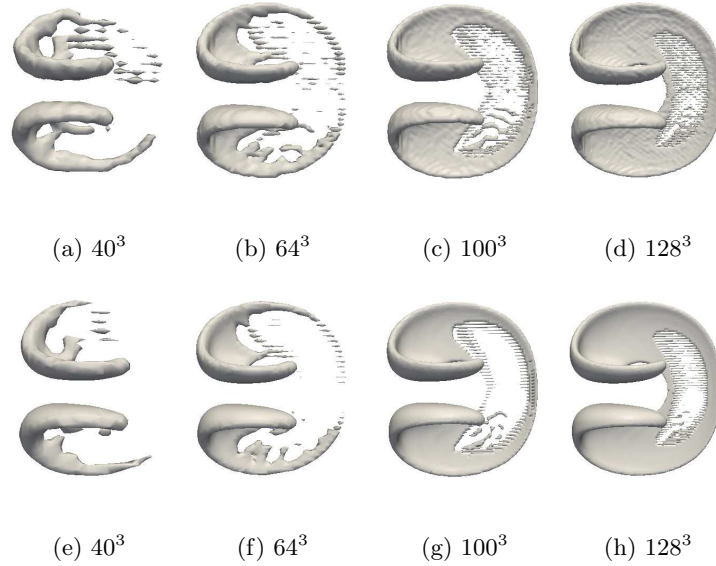


Figure 9: Three-dimensional rotating sphere in a non-uniform flow test for various levels of mesh. The 0.5-iso-surface obtained with the ILSVOF method (top) and without the level set step (bottom) are shown at the maximum deformation time,  $t = T/2$ .

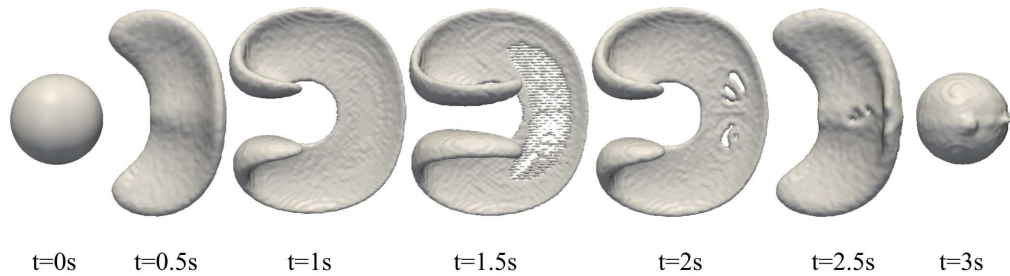


Figure 10: Three-dimensional rotating sphere in a non-uniform flow during time evolution in  $[0, T]$  for a fine hexahedral mesh of  $128^3$  hexahedra.



(a) Developed method (b) Isoface method without (c) Interface compression  
 ILSVOF. level set. scheme, MULES.

Figure 11: Three-dimensional rotating sphere in a non-uniform flow test using the  $128^3$  hexahedral mesh. Initial transparent blue surface at  $t = 0$  and final position of the zero-level set iso-surface solid grey iso-surface at  $t = T$ .

519 *3.3. Three-dimensional dam break case without obstacle*

520 The dam break problem is studied next which consists of a simple three-  
 521 dimensional rectangular geometry wherein a liquid column is initially held still  
 522 by a dam. When the dam is suddenly removed, the liquid column collapses. The  
 523 tank containing the liquid column which collapses in this case is a rectangular

Table 6: Comparison of the methods using tetrahedral meshes for the three-dimensional rotating sphere case.

Mesh resolution	ILSVOF method			VOF method		
	$E_a$	$\min(\alpha)$	$\max(\alpha)$	$E_a$	$\min(\alpha)$	$\max(\alpha)$
163208	$-6.42 \times 10^{-8}$	0	1.0	$2.68 \times 10^{-8}$	0.0	1.0
322676	$-8.7 \times 10^{-3}$	0.0	1.0	$-3.78 \times 10^{-3}$	0.0	1.0
1083126	$-2.3 \times 10^{-4}$	0.0	1.0	$-7.8 \times 10^{-3}$	0.0	1.0

Table 7:  $L_1(\alpha)$  error norm for different meshes for the three-dimensional rotating sphere case and comparison with other numerical methods.

Authors	$32^3$	$64^3$	$128^3$
RK-3D using PLIC [64]	$7.85 \times 10^{-3}$	$2.75 \times 10^{-3}$	$7.41 \times 10^{-4}$
THINC/SW scheme [59]	$8.39 \times 10^{-3}$	$3.47 \times 10^{-3}$	$1.08 \times 10^{-3}$
interFoam [56]	$9.95 \times 10^{-3}$	$4.78 \times 10^{-3}$	$2.03 \times 10^{-3}$
ISLSVOF method	$8.89 \times 10^{-3}$	$2.96 \times 10^{-3}$	$8.06 \times 10^{-4}$

524 domain with dimensions  $4a \times 2.4a \times a$ . For a more convenient comparison,  
525 the fluid in the liquid column is assumed to be water and the rest of the tank  
526 is filled with air. Both fluids are assumed to be initially still, and the physical  
527 properties of the three-dimensional case are shown in Table 8. Initially the liquid  
528 column has dimensions  $a \times 2a \times a$ . The vertical acceleration due to gravity is  
529 taken to be  $9.81 \text{ ms}^{-2}$ . The velocity before removing the dam, is zero for the  
530 liquid column and the air, and the pressure is set to be the hydrostatic pressure.  
531 Free slip boundary conditions are imposed for all the boundaries of the domain  
532 (assuming zero normal velocity and zero tangential traction) except for the  
533 open top boundary (where the tangential velocity and normal traction are zero).  
534 The displacement of the interface between water and air is tracked in order to  
535 characterise the performance of the developed method using three different grids  
536 ( $40 \times 10 \times 20$ ,  $80 \times 20 \times 40$  and  $160 \times 40 \times 80$ ). The results are compared with  
537 the experimental data available in [65] and previous numerical studies using  
538 the LS method from [66] which is a conservative level set method based on the  
539 finite element approach which employs the volume fraction for correcting the  
540 distance function. The results for the position of the water-air interface along  
541 the horizontal (x-axis) and the vertical (y-axis) directions are shown in Fig. 12.  
542 The results for the position are normalised with the length parameter  $a$  and are  
543 plotted against the non-dimensional time. The predictions for the leading-edge  
544 position are in good agreement with the experimental data for the examined  
545 time interval. The accuracy in the predictions for the horizontal direction is  
546 closer initially and reasonably close to the experiment during the simulation  
547 until the leading edge reaches the wall,  $x/a = 4$ . The flow slows down as a  
548 result of wall friction as reported in the experimental work and, as a result, the  
549 calculated interface is expected to differ from the experiment, although this is  
550 less than five to ten percent here for the fine and coarse meshes respectively. The  
551 interface in [66] reaches the position  $x/a = 4$  faster than the present simulations  
552 here. In the method presented here, the liquid front propagates slower than in  
553 [66] although the results in [66] for a coarse mesh (not shown here) had similar  
554 trends as for the results obtained here for the different grids. The coarse grid

555 results in the present study are close to the liquid front results reported in [65],  
 556 with the results obtained with the other two meshes also being reasonably close  
 557 to the experiment. The time evolution of the interface is shown in Figs.13. The  
 558 shape of the interface remains almost flat for the considered time steps of the  
 559 experiment, and in Fig.13(a-c). Once the collapsing liquid column reaches the  
 560 wall, the water rises upwards forming a layer on the right wall. During the time  
 561 interval  $[0, 0.26s]$  the vertical position of the interface decreases as expected, and  
 562 both the present method and the results of Kees et al.[66] are seen to be very  
 563 close in Fig. 12b, having the same rate of change in the liquid column height  
 564 for the different grid resolutions. The fluid percent mass loss evolution for the  
 565 dam break case is shown in Fig. 14. The mass loss approaches zero for the fine  
 566 mesh and remains less than 0.01 percent for the coarse mesh.

Table 8: Physical properties for the dam break case.

	Physical and numerical parameters
Water density	1000 $kg/m^3$
Air density	1.0 $kg/m^3$
Water kinematic viscosity	1.0e-06 $m^2/s$
Air kinematic viscosity	1.0e-04 $m^2/s$
Length a	0.146 $m$
CFL number	0.5



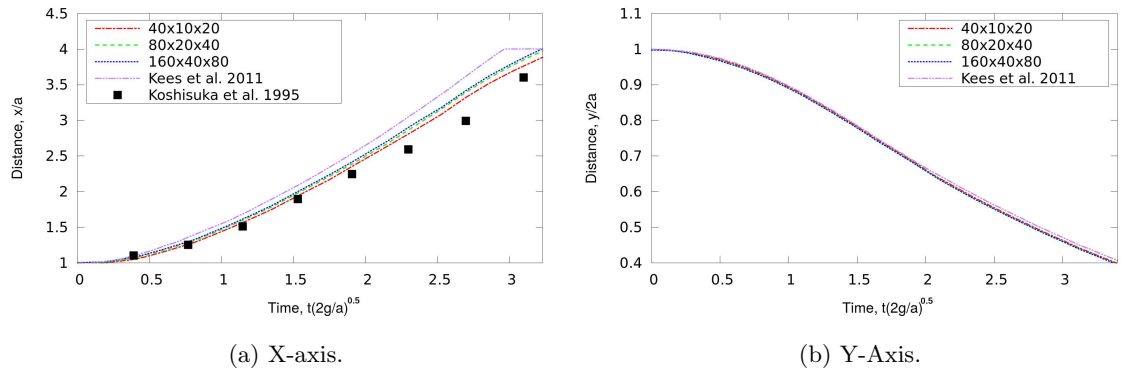


Figure 12: Water-air interface position along the x-axis and y-axis for the three-dimensional dam break case without obstacle.

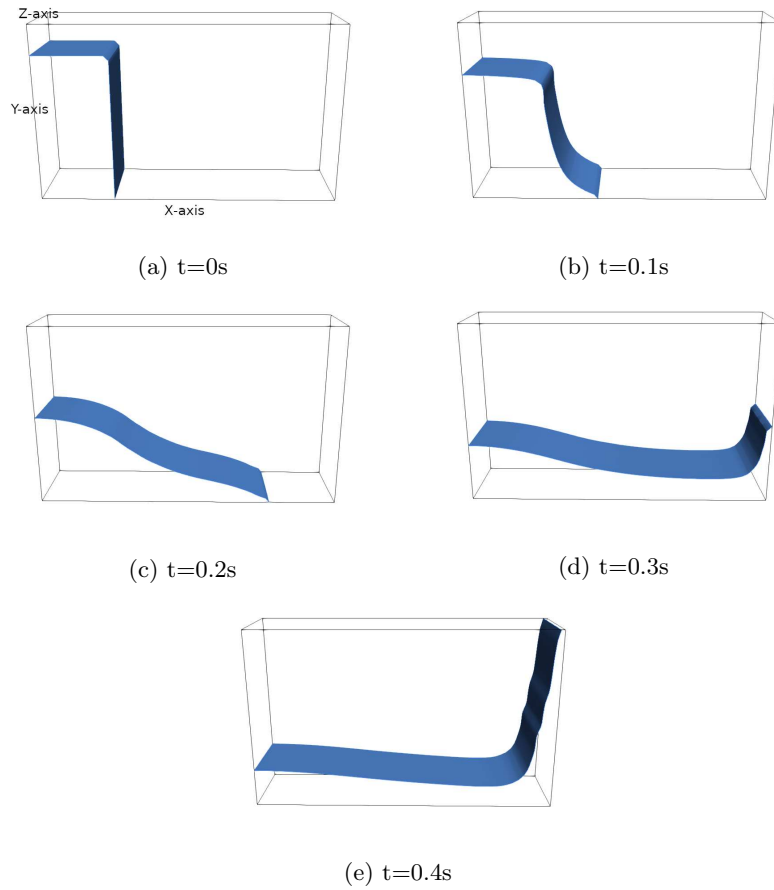


Figure 13: 0.5-isosurface snapshots at different times for the three-dimensional dam break case without obstacle. The liquid column starts to collapse at  $t=0s$  and moves towards the right wall until it impinges and rises up forming a layer that keeps moving upwards until it returns back to the tank due to gravity.

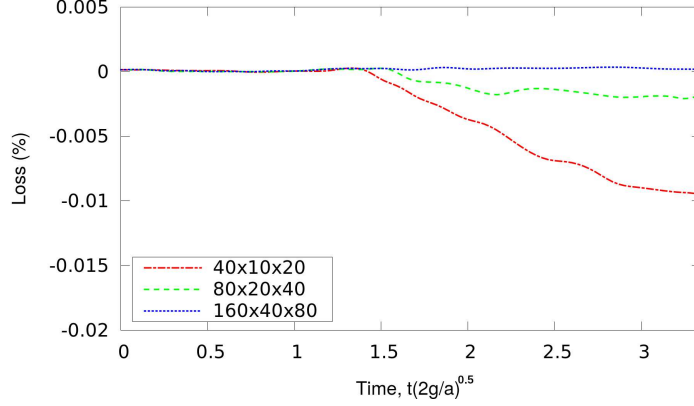


Figure 14: Percent mass loss for the dam break case through time for different mesh resolutions.

### 567 3.4. Static drop

568 In this test case we are interested in the verification of the methodology  
569 for the stationary Laplace solution for a droplet inside a closed domain and  
570 assessing the spurious currents [29, 67]. Neglecting any gravitational effects  
571 and any external forces the interface between the drop and the ambient fluid is  
572 expected to remain at rest. The surface tension force ( $\sigma\kappa$ ) is balanced by the  
573 pressure force at the interface according to Laplace's law:  $\Delta p_{exact} = \sigma\kappa_{exact}$ ,  
574 where the exact interface curvature is  $\kappa = 2/d$  and  $\sigma$  is the surface tension. For  
575 a constant pressure outside the droplet  $p_0$  and zero velocity, the pressure inside  
576 remains constant and equal to  $p_0 + 2\sigma/d$ . Due to spurious currents the calculated  
577 pressure will differ. A  $2d \times 2d$  domain was used for the present numerical tests  
578 with  $d = 0.5cm$  and the density ratio between the droplet and the surroundings  
579 was  $10^4$ . The viscosities inside and outside were equal to 1 and the surface  
580 tension was  $1kg \cdot s^{-2}$ . For the two-dimensional tests, three meshes of triangular  
581 elements were used (with grid size  $\Delta x = 1/25, 1/50, 1/100$  as in [29]). In order  
582 to evaluate the parasitic currents in the domain, the  $L_1$  error norm is calculated  
583 as

$$L_1(\mathbf{u}) = \frac{1}{N_c} \sum_i (\mathbf{u}\mathbf{u})^{1/2} \frac{\mu}{\sigma} \quad (34)$$

584 where the summation is done over the entire domain as in [29] and [68]. The  
 585 pressure ranges from  $p_{out}$  (pressure outside the droplet) to the inside pressure  
 586 ( $p_{in}$ ). The pressure error used to evaluate the pressure jump denoted by  $E(\Delta p)$ ,  
 587 is

$$E(\Delta p) = \frac{|p_{in} - p_{out} - 2\sigma/d|}{2\sigma/d} \quad (35)$$

588 The calculated values for  $L_1$  and  $E(\Delta p)$  for the three meshes are shown in  
 589 Table 9. The results are also compared to the ones obtained using the VOF  
 590 only without using level set and the CLSVOF in [29] using PLIC. The parasitic  
 591 currents obtained here are close to those in [29] and smaller than the VOF ap-  
 592 proach. In all cases the error  $L_1$  decreases when increasing the mesh resolution.  
 593 Similar behaviour is observed for the  $E(\Delta p)$  which remained smaller than the  
 594 calculated error values for pressure jump reported in [29] for the different grid  
 595 resolutions. Fig.15 shows the pressure jump for the three different meshes com-  
 596 pared to the exact solution (normalised with the maximum pressure difference  
 597  $\Delta p_0$ ). Overall the calculated pressure is close enough to the exact value.

598 Another values that are also used for the static drop test are the  $L_1$  error  
 599 norm for pressure,  $L_1(p)$  and the maximum velocity after one and fifty time-  
 600 steps  $U_{max,1}, U_{max,50}$ . The drop density for the test is set to  $1000kgm^{-3}$  with  
 601 a density ratio with the ambient gas phase equal to 1000. The rest of the  
 602 properties for the drop and the outside are set as in [68]. For this test, the  
 603 drop has a radius  $R = 2cm$  and is placed at the centre of a  $6cm \times 6cm$  square  
 604 domain. Three different grid resolutions were used for this case, with grid size  
 605  $\Delta x$  such that  $R/\Delta x = 10, 20, 40$  and the results are shown in Table 10. The  
 606 order for the  $L_1(p)$  error remains at the order of  $10^{-4}$  or below and the accuracy  
 607 of the presented method was close to the CLSVOF works in [68] and [55]. The  
 608 unphysical velocity fields that occur in the areas where pressure changes are  
 609 monitored using the maximum velocity  $U_{max}$ . In this study  $U_{max}$  was of order

Table 9: Comparisons of the methods using unstructured meshes for the two-dimensional static drop case.

Mesh resolution	ILSVOF method		VOF method		CLSVOF using PLIC [29]	
	$L_1(\mathbf{u})$	$E(\Delta p)$	$L_1(\mathbf{u})$	$E(\Delta p)$	$L_1(\mathbf{u})$	$E(\Delta p)$
1/25	$1.24 \times 10^{-4}$	0.011	$5.84 \times 10^{-3}$	0.026	$1.3 \times 10^{-4}$	0.02433
1/50	$9.81 \times 10^{-6}$	0.0046	$3.76 \times 10^{-5}$	0.0078	$3.19 \times 10^{-5}$	0.00651
1/100	$7.46 \times 10^{-6}$	0.0017	$6.61 \times 10^{-5}$	0.0049	$8.82 \times 10^{-6}$	0.00215

610 of  $10^{-8}$  for the coarser mesh and was higher for the finer meshes, at the order of  
 611  $10^{-7}$  as in [67]. Similar patterns for higher parasitic currents while increasing  
 612 the mesh resolution were also reported before in [68], [55] and [67] and has been  
 613 reported for different VOF methods which employ the continuous surface force  
 614 model [50].

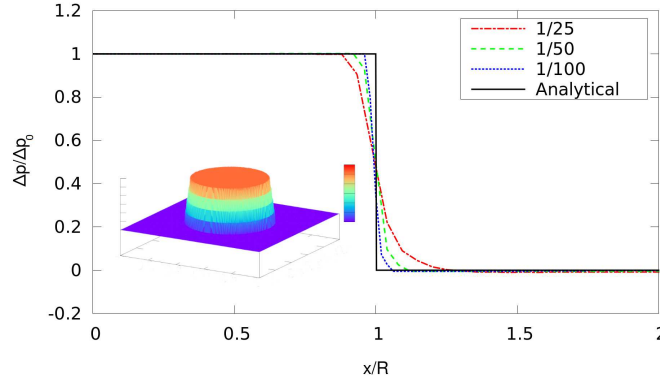


Figure 15: Distribution of the pressure for the static drop test case. Three different mesh resolutions are used to capture the pressure jump across the interface. The pressure is normalised with the exact value  $\Delta p_0$  and the distance with the droplet radius  $R$ . The distribution of the pressure for the finest mesh is also shown.

Table 10: Convergence study for the calculation of pressure, pressure error and velocity for the static drop test. Three different mesh resolutions are used and the density ratio was 1000 on three different grids. Results are compared with different numerical studies.

Authors	$R/\Delta x$	$L_1(p)$	$ u_{max,1} $	$ u_{max,50} $
Gerland et al. 2006 [68]	10	$4.81 \times 10^{-3}$	$7.82 \times 10^{-8}$	$3.91 \times 10^{-6}$
	20	$9.48 \times 10^{-4}$	$1.70 \times 10^{-7}$	$8.53 \times 10^{-6}$
	40	$7.04 \times 10^{-5}$	$4.34 \times 10^{-7}$	$2.17 \times 10^{-5}$
Ningegowda et al. 2014 [55]	10	$1.14 \times 10^{-2}$	$1.12 \times 10^{-6}$	$5.11 \times 10^{-5}$
	20	$7.53 \times 10^{-3}$	$5.88 \times 10^{-6}$	$3.10 \times 10^{-4}$
	40	$2.92 \times 10^{-3}$	$1.30 \times 10^{-5}$	$9.43 \times 10^{-4}$
Jarauta et al. 2018 [67]	10	$1.25 \times 10^{-4}$	$6.08 \times 10^{-9}$	$4.09 \times 10^{-7}$
	20	$3.12 \times 10^{-4}$	$4.38 \times 10^{-8}$	$1.22 \times 10^{-6}$
	40	$7.85 \times 10^{-5}$	$4.26 \times 10^{-7}$	$3.55 \times 10^{-6}$
ISLSVOF method	10	$7.36 \times 10^{-4}$	$2.36 \times 10^{-8}$	$8.89 \times 10^{-6}$
	20	$1.66 \times 10^{-4}$	$5.41 \times 10^{-8}$	$3.46 \times 10^{-6}$
	40	$8.21 \times 10^{-5}$	$7.22 \times 10^{-7}$	$1.17 \times 10^{-6}$

615 *3.5. Rising bubble*

616 The final test case is the rising bubble test proposed in [69]. A circular  
 617 bubble is initially placed in a column filled with fluid of higher density than  
 618 the density of bubble. Due to the buoyancy force, the bubble rises and deforms  
 619 while moving towards the top of the column. The bubble diameter is initially  
 620  $d = 0.5$  units and is centred at  $(0.5, 0.5)$  in a rectangular domain with dimensions  
 621  $2d \times 4d$  as in Fig.16. At the bottom and the top of the column a no-slip boundary  
 622 condition is applied with a free-stream boundary condition at the vertical walls  
 623 of the domain. The velocity is set to zero in the domain, and inside the bubble  
 624 the pressure is constant. The physical properties for the bubble and the heavier  
 625 surrounding fluid are listed in Table 11. Different triangular meshes were used  
 626 with their resolution varying as:  $d/40, d/80, d/160$ . The benchmark quantities  
 627 used by [69] are the centre mass ( $y_c$ ), the rise velocity of the bubble ( $v_c$ ) and its  
 628 circularity or sphericity in three dimensions ( $\zeta$ ). These are defined as

$$\begin{aligned}
 y_c &= \frac{\int_{\Omega_b} \mathbf{x} dV}{\int_{\Omega_b} dV} \\
 v_c &= \frac{\int_{\Omega_b} \mathbf{u} dV}{\int_{\Omega_b} dV} \\
 \zeta &= \frac{\pi d}{\Pi}
 \end{aligned}
 \tag{36}$$

631 where  $\Omega_b$  is the region occupied by the bubble and  $\Pi$  is the perimeter of  
 632 the bubble. Fig.17 shows the benchmark quantities through time for the dif-  
 633 ferent meshes. Results obtained in the present study are close to the values  
 634 obtained in [69] and [70] for  $x_c$ ,  $v_c$  and  $\zeta$  for the different mesh resolutions. For  
 635 the present conditions with  $Re = 35$  and  $Eo = 10$ , where  $Eo = gd^2\Delta\rho/\sigma$  is  
 636 the Eötvös number, the surface tension force is significant which prevents the  
 637 bubble disintegrating. The bubble deforms ( $t = 1$ ) and changes shape from cir-  
 638 cular to ellipsoid (see also [70]) reaching its terminal velocity at  $t = 2$  which is  
 639 approximately 90 percent of the maximum bubble velocity. The change in rise  
 640 velocity is in good agreement with the velocity obtained in [70]. At the change  
 641 in circularity at  $t = 1.9$  where the surface tension effect on the bubble shape is

642 more evident, and is captured with all three computational meshes in this study  
643 and is also in close agreement with the calculated  $\zeta$  in [69]. Similar patterns  
644 for the calculated benchmark quantities were also observed in other numerical  
645 works [29, 33, 70]. The results for the relative error norms for  $y_c$ ,  $\zeta$  and  $v_c$  are  
646 shown in Table 12. The calculated errors are in close agreement with the results  
647 reported in [70] for the three benchmark quantities.

648 For the three-dimensional version of rising bubble test case, a three-dimensional  
649 bubble is placed in a cylinder with height  $8d$  and diameter  $8d$ . The bubble is  
650 placed at a distance  $1.5d$  from the bottom of the cylinder. The density and  
651 viscosity ratio between the bubble and the surrounding fluid were set to 100.  
652 Three hexahedral meshes with different resolution were used for this study,  
653 with a grid size  $\Delta x = d/15, 20, 40$ . The errors  $E_{Re}$  and  $E_\zeta$  for the calculated  
654 Reynolds number  $Re$  and sphericity  $\zeta$  are used to assess the accuracy of the  
655 method, where  $E_{Re} = (Re - Re_{exact})/Re_{exact}$ ,  $E_\zeta = (\zeta - \zeta_{exact})/\zeta_{exact}$  (where  
656  $Re_{exact}$  and  $\zeta_{exact}$  are the exact values for  $Re$  and  $\zeta$  respectively). The results  
657 shown in Table 13 are in good agreement for the three meshes compared to  
658 the results from the reference case in [29]. In Fig.18 the mass conservation  
659 error is shown through time. The mass conservation error is calculated with  
660 respect to the volume fraction at  $t = 0$ ,  $\alpha(0)$  and is defined following [29] as  
661  $\delta M = |\alpha - \alpha(0)|/\alpha(0)$ . The error for the different meshes remained of the order  
662 of  $10^{-5}$  or below showing reasonable accuracy for mass conservation. A similar  
663 order for  $\delta M$  is reported in the CLSVOF work in [29].

Table 11: Physical properties for the two-dimensional rising bubble test case.

	Physical and numerical parameters
Heavy fluid density	1000 $kg/m^3$
Bubble density	100 $kg/m^3$
Heavy fluid viscosity	10 $kg/m \cdot s$
Bubble fluid viscosity	1 $kg/m \cdot s$

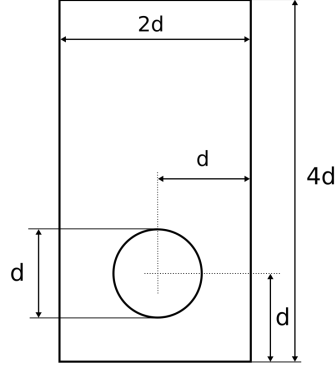


Figure 16: Domain for the two-dimensional bubble rise test case. The diameter of the bubble is initially  $d = 0.5$ .

Table 12: Relative norm error for the centre of mass, circularity and velocity of the bubble in the two-dimensional rising bubble case. Three different structured meshes are used, and the results are compared with the level set method of [70].

Mesh size	ILSVOF method			LS method of [70]		
	Centre of mass	Circularity	Velocity	Centre of mass	Circularity	Velocity
1/40	$1.79 \times 10^{-3}$	$1.19 \times 10^{-3}$	$1.06 \times 10^{-2}$	$2.65 \times 10^{-3}$	$1.0 \times 10^{-3}$	$1.19 \times 10^{-2}$
1/80	$8.91 \times 10^{-4}$	$3.18 \times 10^{-4}$	$1.81 \times 10^{-3}$	$9.64 \times 10^{-4}$	$3.01 \times 10^{-4}$	$2.9 \times 10^{-3}$
1/160	$2.41 \times 10^{-4}$	$6.37 \times 10^{-5}$	$6.21 \times 10^{-4}$	$2.62 \times 10^{-4}$	$8.83 \times 10^{-5}$	$7.73 \times 10^{-4}$

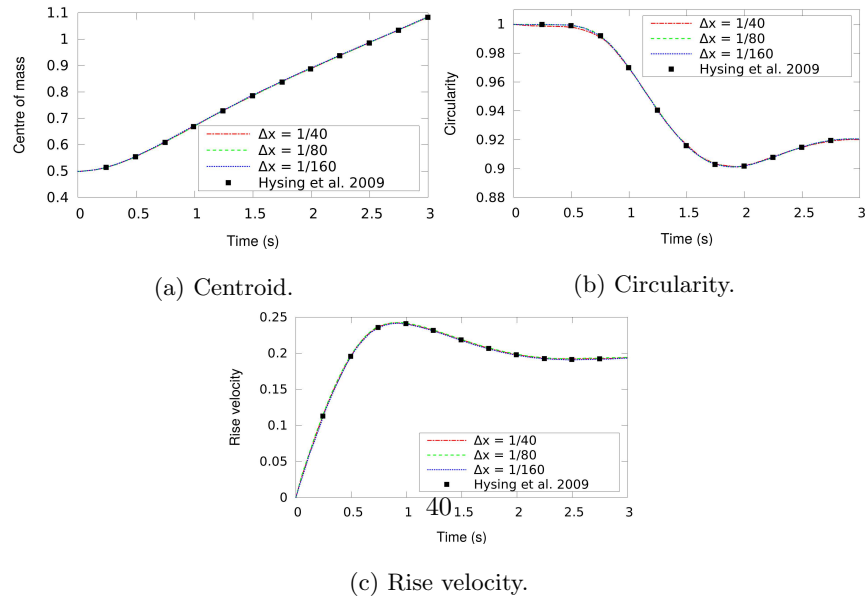


Figure 17: Evolution of rising bubble benchmark quantities through time. The results are compared with the case in [70].



Table 13: Error for Re and sphericity of the bubble in the three-dimensional rising bubble case. Three different structured meshes are used and the results are compared with the CLSVOF method of [29].

Mesh size	ILSVOF method		CLSVOF method of [29]	
	$E_{Re}$	$E_{\zeta}$	$E_{Re}$	$E_{\zeta}$
$d/15$	0.00363	0.0126	0.00341	0.0118
$d/20$	0.00314	0.0063	0.00339	0.0074
$d/40$	0.00271	0.0036	-	-

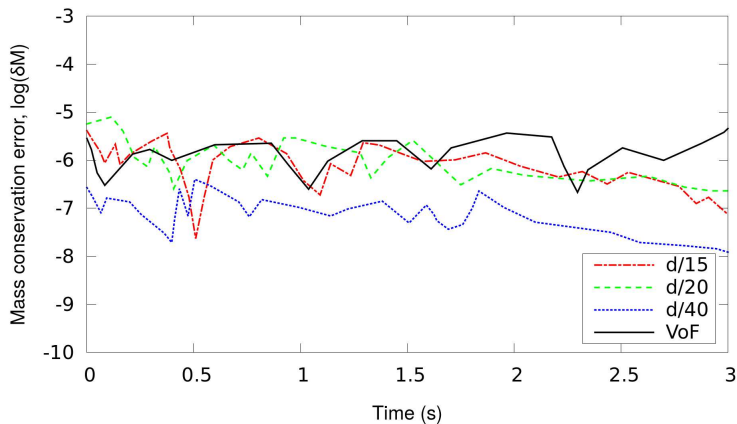


Figure 18: Mass conservation error for three-dimensional rising bubble case for the three levels of refinement.

#### 664 4. Conclusions

665 A novel method for simulating the flow of two immiscible fluids tracking  
666 their interface is presented coupling the level set and volume of fluid methods.  
667 The new ILSVOF method involves a novel re-initialisation methodology which  
668 is described in detail. ILSVOF is simple and can be readily implemented for  
669 any type of polyhedral unstructured mesh. A smooth calculation of the gra-  
670 dient of the LS function is utilised considering the neighbouring cells via an

671 interpolation at the cell-faces. Using these cell-face calculations for each inter-  
672 face cell, it is easy to overcome the limitation of having to arbitrarily define the  
673 upwind and downwind cells. The initial value for the re-distancing algorithm is  
674 obtained via the advection of the isoface within a time step instead of by using  
675 an algebraic method. Overall, the method provides better accuracy compared  
676 to the VOF method in most of the numerical tests considered and has been  
677 demonstrated to give an accurate representation of the interface in both two  
678 and three-dimensional test cases. The mapping of the volume fraction to the  
679 distance function is extremely important for the re-initialisation procedure, and  
680 alternative ways of doing this, such as by employing a special advection step  
681 within each solution time step, should be further investigated. Further com-  
682 parisons with high order level set approaches could also be used to improve the  
683 level set advection step.

#### 684 **Acknowledgments**

685 The authors would like to thank the EU project GENIORS (Project ID:  
686 755171) on GEN IV Integrated Oxide Fuels Recycling Strategies and the EPSRC  
687 project PACIFIC (EP/L018616/1) for funding this research.

#### 688 **References**

- 689 [1] C. W. Hirt, B. D. Nichols, Volume of fluid (vof) method for the dynamics  
690 of free boundaries, *Journal of Computational Physics* 39 (1981) 201 – 225.
- 691 [2] B. Lafaurie, C. Nardone, R. Scardovelli, S. Zaleski, G. Zanetti, Modelling  
692 merging and fragmentation in multiphase flows with surfer, *Journal of*  
693 *Computational Physics* 113 (1994) 134–147.
- 694 [3] R. Scardovelli, S. Zaleski, Direct numerical simulation of free-surface and  
695 interfacial flow, *Annual review of fluid mechanics* 31 (1999) 567–603.

- 696 [4] D. Gueyffier, J. Li, A. Nadim, R. Scardovelli, S. Zaleski, Volume-of-  
697 fluid interface tracking with smoothed surface stress methods for three-  
698 dimensional flows, *Journal of Computational physics* 152 (1999) 423–456.
- 699 [5] R. Scardovelli, S. Zaleski, Analytical relations connecting linear inter-  
700 faces and volume fractions in rectangular grids, *Journal of Computational*  
701 *Physics* 164 (2000) 228–237.
- 702 [6] E. Aulisa, S. Manservigi, R. Scardovelli, S. Zaleski, A geometrical area-  
703 preserving volume-of-fluid advection method, *Journal of Computational*  
704 *Physics* 192 (2003) 355–364.
- 705 [7] G. Tryggvason, R. Scardovelli, S. Zaleski, *Direct numerical simulations of*  
706 *gas–liquid multiphase flows*, Cambridge University Press, 2011.
- 707 [8] G. Agbaglah, S. Delaux, D. Fuster, J. Hoepffner, C. Josserand, S. Popinet,  
708 P. Ray, R. Scardovelli, S. Zaleski, Parallel simulation of multiphase flows  
709 using octree adaptivity and the volume-of-fluid method, *Comptes Rendus*  
710 *Mecanique* 339 (2011) 194–207.
- 711 [9] M. Owkes, O. Desjardins, A computational framework for conservative,  
712 three-dimensional, unsplit, geometric transport with application to the  
713 volume-of-fluid (vof) method, *Journal of Computational Physics* 270 (2014)  
714 587–612.
- 715 [10] Y. Ling, S. Zaleski, R. Scardovelli, Multiscale simulation of atomization  
716 with small droplets represented by a lagrangian point-particle model, *Inter-*  
717 *national Journal of Multiphase Flow* 76 (2015) 122–143.
- 718 [11] S. Bnà, S. Manservigi, R. Scardovelli, P. Yecko, S. Zaleski, Vofia library to  
719 initialize the volume fraction scalar field, *Computer Physics Communica-*  
720 *tions* 200 (2016) 291–299.
- 721 [12] S. Osher, J. A. Sethian, Fronts propagating with curvature-dependent  
722 speed: Algorithms based on hamilton-jacobi formulations, *Journal of Com-*  
723 *putational Physics* 79 (1988) 12–49.

- 724 [13] B. Merriman, J. K. Bence, S. J. Osher, Motion of multiple junctions: A  
725 level set approach, *Journal of Computational Physics* 112 (1994) 334–363.
- 726 [14] Y.-C. Chang, T. Hou, B. Merriman, S. Osher, A level set formulation of  
727 eulerian interface capturing methods for incompressible fluid flows, *Journal*  
728 *of computational Physics* 124 (1996) 449–464.
- 729 [15] J. A. Sethian, *Level set methods, evolving interfaces in geometry, fluid me-*  
730 *chanics computer vision, and materials sciences*, Cambridge Monographs  
731 *on Applied and Computational Mathematics*, 3 (1996).
- 732 [16] J. A. Sethian, *Level set methods and fast marching methods: evolving*  
733 *interfaces in computational geometry, fluid mechanics, computer vision,*  
734 *and materials science*, volume 3, Cambridge university press, 1999.
- 735 [17] S. Osher, R. P. Fedkiw, *Level set methods: an overview and some recent*  
736 *results*, *Journal of Computational physics* 169 (2001) 463–502.
- 737 [18] D. Enright, R. Fedkiw, J. Ferziger, I. Mitchell, A hybrid particle level  
738 set method for improved interface capturing, *Journal of Computational*  
739 *physics* 183 (2002) 83–116.
- 740 [19] J. A. Sethian, P. Smereka, *Level set methods for fluid interfaces*, *Annual*  
741 *review of fluid mechanics* 35 (2003) 341–372.
- 742 [20] S. Osher, R. Fedkiw, *Level set methods and dynamic implicit surfaces*,  
743 volume 153, Springer Science & Business Media, 2006.
- 744 [21] J. A. Sethian, A. Wiegmann, *Structural boundary design via level set and*  
745 *immersed interface methods*, *Journal of computational physics* 163 (2000)  
746 489–528.
- 747 [22] S. Osher, N. Paragios, *Geometric level set methods in imaging, vision, and*  
748 *graphics*, Springer Science & Business Media, 2003.
- 749 [23] R. Malladi, J. A. Sethian, *Image processing via level set curvature flow*,  
750 *proceedings of the National Academy of sciences* 92 (1995) 7046–7050.

- 751 [24] W. Dawes, S. Harvey, W. Kellar, Using level sets as the basis for a scal-  
752 able, parallel geometry engine and mesh generation system, in: 47th  
753 AIAA Aerospace Sciences Meeting including The New Horizons Forum and  
754 Aerospace Exposition, 2009, p. 372.
- 755 [25] M. K. Cameron, S. B. Fomel, J. A. Sethian, Seismic velocity estimation  
756 from time migration, *Inverse Problems* 23 (2007) 1329.
- 757 [26] J. A. Sethian, Y. Shan, Solving partial differential equations on irregular  
758 domains with moving interfaces, with applications to superconformal elec-  
759 trodeposition in semiconductor manufacturing, *Journal of Computational*  
760 *Physics* 227 (2008) 6411–6447.
- 761 [27] A. Bourlioux, A coupled level set and volume of fluid algorithm for tracking  
762 material interfaces, *Proceedings of the 6th International Symposium On*  
763 *Computational Fluid Dynamics* 6 (1995) 15–22.
- 764 [28] M. Sussman, E. G. Puckett, A coupled level set and volume-of-fluid method  
765 for computing 3d and axisymmetric incompressible two-phase flows, *Jour-*  
766 *nal of Computational Physics* 162 (2000) 301–337.
- 767 [29] N. Balcázar, O. Lehmkuhl, L. Jofre, J. Rigola, A. Oliva, A coupled volume-  
768 of-fluid/level-set method for simulation of two-phase flows on unstructured  
769 meshes, *Computers and Fluids* 124 (2016) 12 – 29.
- 770 [30] Z. Cao, D. Sun, J. Wei, B. Yu, A coupled volume-of-fluid and level set  
771 method based on multi-dimensional advection for unstructured triangular  
772 meshes, *Chemical Engineering Science* 176 (2018) 560 – 579.
- 773 [31] D. L. Sun, W. Q. Tao, A coupled volume-of-fluid and level set (voset)  
774 method for computing incompressible two-phase flows, *International Jour-*  
775 *nal of Heat and Mass Transfer* 53 (2010) 645 – 655.
- 776 [32] Y. Zhao, H. C. Chen, A new coupled level set and volume-of-fluid method  
777 to capture free surface on an overset grid system, *International Journal of*  
778 *Multiphase Flow* 90 (2017) 144 – 155.

- 779 [33] N. K. Singh, B. Premachandran, A coupled level set and volume of fluid  
780 method on unstructured grids for the direct numerical simulations of two-  
781 phase flows including phase change, *International Journal of Heat and Mass*  
782 *Transfer* 122 (2018) 182 – 203.
- 783 [34] M. Dianat, M. Skarysz, A. Garmory, A coupled level set and volume of  
784 fluid method for automotive exterior water management applications, *In-*  
785 *ternational Journal of Multiphase Flow* 91 (2017) 19 – 38.
- 786 [35] E. Olsson, G. Kreiss, A conservative level set method for two phase flow,  
787 *Journal of Computational Physics* 210 (2005) 225–246.
- 788 [36] A. Albadawi, D. B. Donoghue, A. J. Robinson, D. B. Murray, Y. M. C.  
789 Delaur, Influence of surface tension implementation in volume of fluid  
790 and coupled volume of fluid with level set methods for bubble growth and  
791 detachment, *International Journal of Multiphase Flow* 53 (2013) 11 – 28.
- 792 [37] T. Pringuey, Large eddy simulation of primary liquid sheet breakup, Ph.D.  
793 thesis, University of Cambridge, 2012.
- 794 [38] L. H. Zhao, J. Mao, X. Q. Liu, X. Bai, J. Willims, Improved conservative  
795 level set method for free surface flow simulation, *Journal of Hydrodynamics,*  
796 *Ser. B* 26 (2014) 316 – 325.
- 797 [39] M. Sussman, P. Smereka, S. Osher, A level set approach for computing so-  
798 lutions to incompressible two-phase flow, *Journal of Computational Physics*  
799 114 (1994) 146–159.
- 800 [40] G. Russo, P. Smereka, A remark on computing distance functions, *Journal*  
801 *of Computational Physics* 163 (2000) 51–67.
- 802 [41] D. Hartmann, M. Meinke, W. Schröder, Differential equation based con-  
803 strained reinitialization for level set methods, *Journal of Computational*  
804 *Physics* 227 (2008) 6821 – 6845.

- 805 [42] J. Roenby, H. Bredmose, H. Jasak, A computational method for sharp  
806 interface advection, Royal Society open science (2016).
- 807 [43] H. G. Weller, G. Tabor, H. Jasak, C. Fureby, A tensorial approach to com-  
808 putational continuum mechanics using object-oriented techniques, Comput.  
809 Phys. 12 (1998) 620–631.
- 810 [44] X. D. Liu, S. Osher, T. Chan, Weighted essentially non-oscillatory schemes,  
811 Journal of Computational Physics 115 (1994) 200–212.
- 812 [45] H. Weller, A new approach to vof-based interface capturing methods for in-  
813 compressible and compressible flow, OpenCFD Ltd technical report (2008).
- 814 [46] A. Prosperetti, G. Tryggvason, Computational Methods for Multiphase  
815 Flow, Cambridge University Press, 2009.
- 816 [47] D. Hartmann, M. Meinke, W. Schröder, The constrained reinitialization  
817 equation for level set methods, Journal of Computational Physics 229  
818 (2010) 1514–1535.
- 819 [48] C. Dapogny, P. Frey, Computation of the signed distance function to a  
820 discrete contour on adapted triangulation, Calcolo 49 (2012) 193–219.
- 821 [49] C. Kunkelmann, P. Stephan, Modification and extension of a standard  
822 volume-of-fluid solver for simulating boiling heat transfer, ECCOMAS  
823 CFD2010, 2010.
- 824 [50] J. U. Brackbill, D. B. Kothe, C. Zemach, A continuum method for modeling  
825 surface tension, Journal of computational physics 100 (1992) 335–354.
- 826 [51] M. Rudman, Volume-tracking methods for interfacial flow calculations,  
827 International Journal for Numerical Methods in Fluids 24 (1997) 671–691.
- 828 [52] N. Ashgriz, J. Y. Poo, Flair: Flux line-segment model for advection and  
829 interface reconstruction, Journal of Computational Physics 93 (1991) 449  
830 – 468.

- 831 [53] J. E. Pilliod, E. G. Puckett, Second-order accurate volume-of-fluid algo-  
832 rithms for tracking material interfaces, *Journal of Computational Physics*  
833 199 (2004) 465 – 502.
- 834 [54] R. J. LeVeque, High-resolution conservative algorithms for advection in  
835 incompressible flow, *SIAM J. Numer. Anal.* 33 (1996) 627–665.
- 836 [55] B. Ningegowda, B. Premachandran, A coupled level set and volume of fluid  
837 method with multi-directional advection algorithms for two-phase flows  
838 with and without phase change, *International Journal of Heat and Mass*  
839 *Transfer* 79 (2014) 532–550.
- 840 [56] S. S. Deshpande, L. Anumolu, M. F. Trujillo, Evaluating the performance  
841 of the two-phase flow solver interfoam, *Computational Science & Discovery*  
842 5 (2012) 014016.
- 843 [57] K. Yokoi, Efficient implementation of thinc scheme: a simple and practical  
844 smoothed vof algorithm, *Journal of Computational Physics* 226 (2007)  
845 1985–2002.
- 846 [58] B. Xie, F. Xiao, Toward efficient and accurate interface capturing on arbi-  
847 trary hybrid unstructured grids: The thinc method with quadratic surface  
848 representation and gaussian quadrature, *Journal of Computational Physics*  
849 349 (2017) 415–440.
- 850 [59] F. Xiao, S. Ii, C. Chen, Revisit to the thinc scheme: a simple algebraic vof  
851 algorithm, *Journal of Computational Physics* 230 (2011) 7086–7092.
- 852 [60] M. Jemison, E. Loch, M. Sussman, M. Shashkov, M. Arienti, M. Ohta,  
853 Y. Wang, A coupled level set-moment of fluid method for incompressible  
854 two-phase flows, *Journal of Scientific Computing* 54 (2013) 454–491.
- 855 [61] W. J. Rider, D. B. Kothe, Reconstructing volume tracking, *Journal of*  
856 *computational physics* 141 (1998) 112–152.



- 857 [62] J. Lopez, J. Hernandez, P. Gomez, F. Faura, An improved plic-vof method  
858 for tracking thin fluid structures in incompressible two-phase flows, *Journal*  
859 *of Computational Physics* 208 (2005) 51–74.
- 860 [63] T. Ménard, S. Tanguy, A. Berlemont, Coupling level set/vof/ghost fluid  
861 methods: Validation and application to 3d simulation of the primary break-  
862 up of a liquid jet, *International Journal of Multiphase Flow* 33 (2007) 510  
863 – 524.
- 864 [64] J. Hernández, J. López, P. Gómez, C. Zanzi, F. Faura, A new volume  
865 of fluid method in three dimensionspart i: Multidimensional advection  
866 method with face-matched flux polyhedra, *International Journal for Nu-*  
867 *merical Methods in Fluids* 58 (2008) 897–921.
- 868 [65] S. Koshizuka, Y. Oka, Moving-particle semi-implicit method for fragmen-  
869 tation of incompressible fluid, *Nuclear Science and Engineering* 123 (1996)  
870 421–434.
- 871 [66] C. E. Kees, I. Akkerman, M. W. Farthing, Y. Bazilevs, A conservative level  
872 set method suitable for variable-order approximations and unstructured  
873 meshes, *J. Comput. Phys.* 230 (2011) 4536–4558.
- 874 [67] A. Jarauta, P. Ryzhakov, J. Pons-Prats, M. Secanell, An implicit surface  
875 tension model for the analysis of droplet dynamics, *Journal of Computa-*  
876 *tional Physics* 374 (2018) 1196–1218.
- 877 [68] D. Gerlach, G. Tomar, G. Biswas, F. Durst, Comparison of volume-of-  
878 fluid methods for surface tension-dominant two-phase flows, *International*  
879 *Journal of Heat and Mass Transfer* 49 (2006) 740–754.
- 880 [69] S.-R. Hysing, S. Turek, D. Kuzmin, N. Parolini, E. Burman, S. Ganesan,  
881 L. Tobiska, Quantitative benchmark computations of two-dimensional bub-  
882 ble dynamics, *International Journal for Numerical Methods in Fluids* 60  
883 (2009) 1259–1288.

- 884 [70] S. Hysing, Mixed element fem level set method for numerical simulation of  
885 immiscible fluids, *Journal of Computational Physics* 231 (2012) 2449–2465.